

Modular Multi-Rotors: From Quadrotors to Fully-Actuated Aerial Vehicles

Jiawei Xu, Diego S. D'Antonio, and David Saldaña

Abstract—Traditional aerial vehicles have specific characteristics to perform specific tasks but designing a versatile vehicle that can adapt depending on the task is still a challenge. Based on modularity, we propose an aerial robotic system that can increase its payload capacity and actuated degrees of freedom by reconfiguring heterogeneous modules to adapt to different task specifications. The system consists of cuboid modules propelled by quadrotors with tilted rotors. We present two module designs with different actuation properties. By assembling different types of modules, H-ModQuad can increase its actuated degrees of freedom from 4 to 5 and 6 depending on its configuration. By extending the concept of actuation ellipsoids, we find the body frame of a vehicle with which the controller can maximize the maximum thrust. We use polytopes to represent the actuation capability of the vehicles and examine them against task requirements. We derive the modular vehicles' dynamics and propose a general control strategy that applies for all possible numbers of actuated degrees of freedom. The design is validated with simulations and experiments using actual robots, showing that the modular vehicles provide different actuation properties.

Index Terms—Aerial Systems; Mechanics and Control, Motion Control, Redundant Robots, Modular Robots

I. INTRODUCTION

RESEARCH on unmanned aerial vehicles (UAVs) thrives in recent years, offering low-cost solutions for a wide spectrum of applications such as aerial photography [1], [2], object transportation [3], [4], and construction [5], [6]. However, one of their major problems is the lack of versatility. There are two characteristics of versatility on which we would like to focus, the *strength* and the *actuated degrees of freedom (ADOF)*. For instance, in object transportation, the robot hardware design depends on the weight and dimensions of the target payload [7], [8]. An under-powered UAV may not be able to transport a heavy payload timely and safely. While an oversized UAV can carry both large and small objects, it suffers from higher energy consumption and limited motion capability in environments with obstacles. Having additional ADOF is the other desirable property for UAVs. For instance, a traditional quadrotor exhibits a controllable system with four co-linear rotors as actuators [9]. Existing solutions choose to control the three positional DOF and one DOF in the yaw angle of a quadrotor [10]–[12], making such systems under-actuated and require to tilt for horizontal translation. Adding redundant vertical rotors to a quadrotor [13], or connecting multiple modular quadrotors without changing the rotors' orientation [14], do not increase the number of ADOF. As long

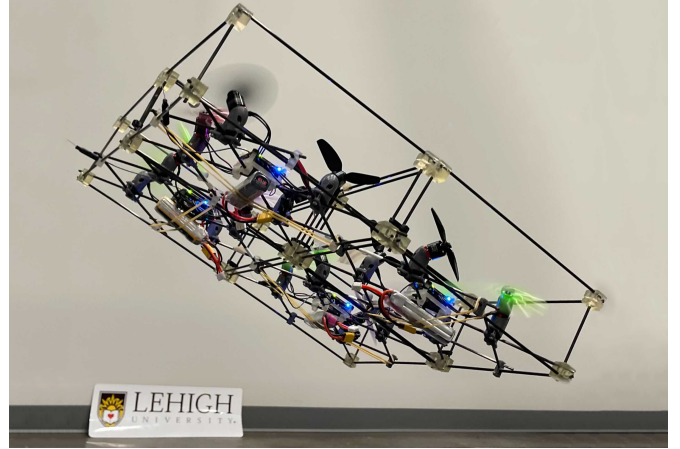


Fig. 1: Four heterogeneous torque-balanced modules of two types forming an 2-by-2 H-ModQuad structure. Each type of modules are diagonally placed in the structure. Considering only the orientations of the rotors, if we rotate one type of the modules along yaw for 90 degrees, the two types of modules become identical. This structure is used in Experiment VII-B, and the picture is captured during its flight.

as all rotors are vertical and pointing in the same direction, it remains impossible for the vehicles to translate horizontally without tilting.

To deal with the limit of under-actuation, one approach is increasing the number of rotors in a multi-rotor vehicle and changing their orientation [15]. The rotor orientation can be either fixed (passive) or changing actively. The problem with actively-tilting rotors is that the tilting mechanism increases the weight and the higher complexity of the vehicle and controller design such as the articulated aerial robot developed in [16]. The work in [17] provides a universal control strategy for both under-actuated and fully-actuated UAVs, but the design of the UAV is specific for certain tasks, which limits the versatility of each individual UAV design.

Modular aerial robots offer a versatile and scalable way to increase their strength [14], [18], [19], and capabilities [20]–[22]. When the task changes, a modular robot can adapt to new requirements by either adding modules, reconfiguring, or changing the type of modules. While homogeneous modules can increase the total force, more modules also add more redundancy to the system, which provides enhanced robustness against mechanical deficiency from the vehicle. Furthermore, modular robots can adapt to new task requirements without changing the design of individual modules [23], [24]. To

J. Xu, D. D'Antonio, and D. Saldaña are with the Autonomous and Intelligent Robotics Laboratory (AIRLab), Lehigh University, PA, USA: {jix519, diego.s.dantonio, saldana}@lehigh.edu

tackle a transportation task, a modular UAV can change the number of modules composing the vehicle to adapt to different payload weights of, for example, a pizza versus a piano. For maintenance tasks such as drilling a hole in a wall, the vehicle would reconfigure to enhance its actuation for independent translation, *i.e.*, although the number of ADOF may remain the same after the reconfiguration, the maximum force that the vehicle can generate in a selected direction increases.

Contribution: The main contribution of this paper is threefold. First, we propose a modular robot composed of individual modules that can fly autonomously. By assembling multiple modules, the vehicle can increase its strength and the number of ADOF from 4 to 5 and 6. Second, we extend the concept of actuation ellipsoids and actuation polytopes to find the body frame along the z -axis of which the vehicle can maximize the maximum thrusting force while maintaining attitude. We propose a set of control strategies that integrate the modular controllers for each number of actuated degrees of freedom. Third, we provide the geometric representation of the actuation capability of a multi-rotor vehicle, and show how to use the representation to compare different vehicle designs against possible tasks.

Different from our previous discussion on H-ModQuad [25], the present paper introduces a novel design, termed the T -module. The unique rotor configuration of our T -module, with rotors pointing in different directions, endows it with enhanced torque generation in the yaw angle compared to conventional quadrotors and our previously introduced R -modules. Despite the existence of similar module designs in the literature [26]–[28], we emphasize that the assembly of heterogeneous T - and/or R -modules in various configurations yields new actuation capabilities, such as full actuation, on assembled vehicles, surpassing those of individual quadrotor modules. Consequently, users can optimize vehicle configurations to meet specific task requirements with a limited number of module types. Our contribution extends to the introduction of an analysis method for the actuation capabilities of multi-rotors based on computational geometry, represented as 6-D polytopes in the wrench space. Compared to force envelopes [17], [29], [30], our actuation polytopes account for realistic constraints such as the uni-directionality of the motors and the coupling relation of the force and torque space. Examining these polytopes for vehicles with different designs allows us to check the suitability of a vehicle configuration for specific task requirements. To enhance computational efficiency, we introduce an optimization-based method as an alternative to the polytope analysis, eliminating the need for high-dimensional convex hull generation and, consequently, improving computational efficiency.

II. RELATED WORK

There are different multi-rotor designs with different characteristics related to the versatility problem in the literature. We provide a short review on the existing designs. A brief taxonomy diagram based on whether the design is able to adapt to different tasks, their modularity, and their ADOF, are shown in Fig. 2.

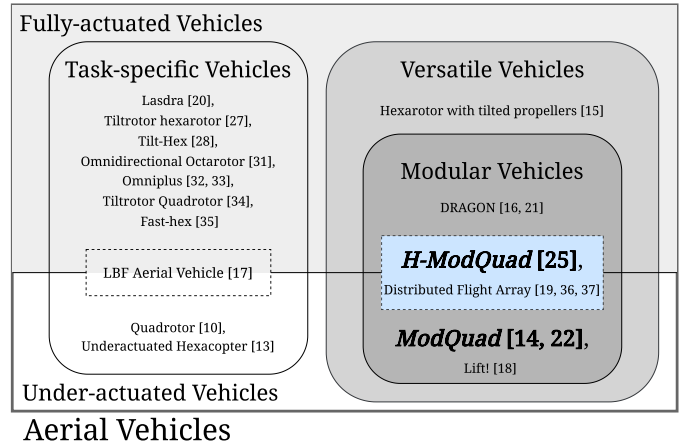


Fig. 2: The taxonomy diagram of all aerial vehicle designs referred to in this paper. We consider their characteristics of versatility, modularity, and ADOF. We highlighted the designs that share the same convention with this paper with its name. Note that our modular multi-rotor vehicle design finds its classification in the shaded cell as a *modular versatile design that can change its ADOF*.

A traditional quadrotor belongs to the category of under-actuated vehicles that are task-specific, limited by its payload capacity and ADOF. A straight-forward way of increasing its payload limit is to increase the number of rotors in the vehicle such as the hexarotor design in [13]. Since the hexarotor has all the rotors statically mounted in co-linear configuration, this design is still under-actuated. In [15], the authors introduced the design and control strategy for a hexarotor with tiltable rotors. Using 6 uni-directional rotors, the vehicle can actuate up to 6 degrees of freedom. The authors provide an optimization metric on the tilting angles of the motors so that when following a trajectory, the multi-rotor minimizes the energy consumption. However, the optimal tilting angles are trajectory-dependent, meaning that if the desired trajectory changes, the tilting angles need to be re-optimized, which limits the versatility of this vehicle. Brescianini and D’Andrea [31] present a multi-rotor design that achieves omnidirectional motion with 8 bi-directional motors. The deployment of reversible motors in this design makes the vehicle work with the controller for fully-actuated multi-rotor vehicles without modification to input allocation strategy. This design enables the multi-rotor vehicle to hover at an arbitrary attitude, which is at the cost of the complexity in motor and frame placement. The work in [32], [33] presents a multi-rotor system that attains omnidirectionality with no less than 7 uni-directional motors. The authors formally show the criteria that define the omnidirectionality for a multi-rotor vehicle. Tognon and Franchi [32] show that by exploring the null space of the allocation matrix which maps the rotor input forces to the local force and torque, the controller can guarantee non-negative thrust forces for all rotors, which makes sure the desired states are achievable by uni-directional motors. Hamandi et al. [33] provide an optimization procedure on the motor placement that minimizes the control input.

As an alternative to increasing the number of rotors to increase the number of ADOF, Ryll et al. [34] propose a control design for a quadrotor with actively tilting rotors. The authors point out that by actively tilting rotors, the rank of the allocation matrix which maps the motor inputs to the output local force and torque does not increase, making the desired input not obtainable with simple matrix operations. Thus, they derive a dynamic output linearization method, which gives a new full-rank mapping from the higher order of motor inputs to the vehicle states. Using the linearization method, one can obtain the desired motor inputs despite the allocation matrix. In [35] is demonstrated a hybrid design where a hexarotor can transit from under-actuated to fully-actuated by using an additional servo motor to tilt the rotors synchronously. By using six motors, the vehicle can transit between under-actuation and full-actuation, making it possible for the vehicle to choose operation modes between high efficiency and full-actuation in-flight. However, those designs of vehicles are fixed in structure, meaning that the vehicles are limited in actuation once constructed and deployed. Given a new task that is beyond their original actuation capabilities, the vehicles are unable to satisfy the task requirements without a full reconstruction, which constrains the versatility of these designs.

We consider modularity a key characteristic of the vehicle design to be versatile. The works in [36], [37] present a hexagonal module that assembles to become a flight array. Each module consists of a rotor and three wheels that help to assemble on the ground. Upon assembly, the flight array composed of multiple modules can fly with a distributed sensing and control strategy. The authors focus on the module design, and the assembled flight array gains redundancy and strength but not additional controllability with more modules. Garanger et al. [38] develop a novel modular multi-rotor system where tetrahedron-shaped quadrotors are used as the elementary module of an aerial vehicle. Four tetrahedron-shaped submodules of one rotor composes one tetracopter which are validated through experiments. By assembling the submodules in various configurations, one group of tetracoverters can increase its ADOF. By self-assembling, the strength scales up. However, the work is currently not focusing on improving the motion capability of the vehicle but the fractal assembly since a minimal unit of the vehicle is unable to achieve autonomous flight. Saldaña et al. [14] introduce the design and implementation of a cuboid modular aerial vehicle that flies independently and is able to assemble with other modules in the air to form a larger structure. The authors showed that the modules can assemble to any shape without losing stability, or disassemble from any shape to smaller structures, all in-flight. Having more homogeneous modules in a structure in this way grants additional redundancy and higher payload capacity, but keeping the same ADOF because all the rotor forces are parallel. Wu et al. [39] show that by connecting bi-copter modules with tilting rotors, the assembled multi-rotor vehicle can increase the load capacity and the ADOF to meet different mission requirements. However, the additional servo motor and vector platform increase the mechanical complexity of the system. These modular vehicle designs are able to

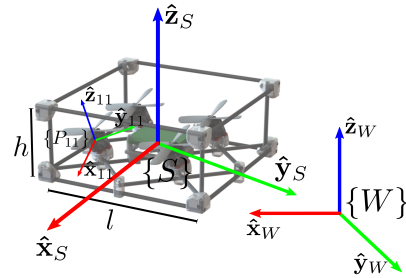


Fig. 3: A R -module with its coordinate frames, and dimensions. Note that this module composes a structure, thus $\{S\}$ aligns with $\{M_1\}$. In Section VI, we will define F -frame. In this example, the F -frame of the structure aligns with $\{P_{11}\}$.

adapt different task such as transporting heavier payloads and following trajectories of higher DOF. Therefore, we consider them versatile vehicles.

Among existing literature, researchers have made efforts increasing the actuation capabilities and versatility of multi-rotor vehicles by deploying novel designs, applying non-linear controllers, and utilizing modularity. Yet, few designs have considered using modular robots to compose large structures that can adapt to various tasks without vehicle reconstruction or additional mechanical components. In this work, we seek to fill this gap by presenting a versatile modular multi-rotor vehicle composed of heterogeneous modules that can achieve a varying number of ADOF which can be applied to solve a variety of problems with different task requirements.

III. PROBLEM STATEMENT

Our work is focused on modular multi-rotor vehicles composed of n independent modules, denoted by the set $\mathcal{M} = \{M_1, M_2, \dots, M_n\}$.

Definition 1 (Module). A module is an autonomous vehicle that is composed of a quadrotor within a cuboid frame. We refer to the square faces of the frame as the top and bottom and the rectangular faces we refer to as the sides. The rotors do not necessarily have to be vertical with respect to the base of the module, and their orientation defines the actuation properties of the module.

Each module $M_i \in \mathcal{M}$ has a mass m_i and an inertia tensor \mathbf{J}_i . A module can dock to another by aligning their sides to create a rigid connection. By performing multiple docking actions, we can assemble a *structure*.

Definition 2 (Structure). A structure is a set of $n \geq 1$ rigidly connected modules forming a single multi-rotor vehicle. Its inertia tensor is denoted by \mathbf{J} and its mass is denoted by m .

We denote the standard basis in \mathbb{R}^3 by $\hat{x} = [1, 0, 0]^T$, $\hat{y} = [0, 1, 0]^T$, and $\hat{z} = [0, 0, 1]^T$. The world coordinate frame, $\{W\}$, is fixed, and its z -axis points upwards. The i -th module in the structure has a module reference frame, $\{M_i\}$, with its origin in the module's center of mass. We define the "front" direction of the module as the x -axis and the "up" direction as the z -axis. The four rotors are in a square configuration and

located on the xy -plane of $\{M_i\}$, with rotor 1, 2, 3, 4 located in the Quadrant 2, 3, 4, 1. Each rotor has a rotor frame with its z -axis pointing in the direction of the rotor force and its x -axis in parallel with the xz -plane of $\{M_i\}$ when not rotating. The orientation of the j -th rotor frame, $\{P_{ij}\}$, in the i -th module frame, $\{M_i\}$, is specified by the rotation matrix ${}^iR_j \in \text{SO}(3)$. A rotation matrix \mathbf{R} can be converted from Euler angles with

$$\mathbf{R} = \begin{bmatrix} c\psi c\theta - s\phi s\psi s\theta & -c\phi s\psi & c\psi s\theta + c\theta s\phi s\psi \\ c\theta s\psi + c\psi s\phi s\theta & c\phi c\psi & s\psi s\theta - c\psi c\theta s\phi \\ -c\phi s\theta & s\phi & c\phi c\theta \end{bmatrix} \quad (1)$$

where ϕ , θ , and ψ represent the corresponding roll-pitch-yaw Euler angles of the frame in the reference frame and $c\theta$ and $s\theta$ denote $\cos \theta$ and $\sin \theta$, respectively, similarly for ϕ and ψ . In a traditional quadrotor, the rotors are oriented vertically, parallel to the z -axis of the quadrotor. In our case, the rotors can be pointing in different directions. The associated coordinate frames of a module are illustrated in Fig. 3. The structure frame, denoted by $\{S\}$, has its origin in its center of mass. Without loss of generality, we align all the module frames in the structure and define the x -, y - and z -axes of $\{S\}$ as in parallel to the x -, y - and z -axes of all modules in the structure. The location and the orientation of $\{S\}$ in the world frame $\{W\}$ is specified by the vector $\mathbf{r} \in \mathbb{R}^3$ and the rotation matrix ${}^WR_S \in \text{SO}(3)$.

The rotation of the rotors $j \in \{1, \dots, 4\}$ in module i generates a thrust $f_{ij} \in [0, f_{max}]$, and a torque from the air drag. The force and torque vectors in $\{M_i\}$, as a function of the thrust f_{ij} , are

$$\mathbf{f}_{ij} = f_{ij} {}^iR_j \hat{\mathbf{z}}, \text{ and } \boldsymbol{\tau}_{ij} = f_{ij} (-1)^j \frac{k_m}{k_f} {}^iR_j \hat{\mathbf{z}},$$

where k_f and k_m are coefficients that can be obtained experimentally.

The structure generates a total force \mathbf{f} and torque $\boldsymbol{\tau}$ in the structure frame $\{S\}$ which can be expressed as the vector summation of all local forces and torques,

$$\mathbf{f} = \sum_{ij} {}^SR_i \mathbf{f}_{ij}, \quad (2)$$

$$\boldsymbol{\tau} = \sum_{ij} \boldsymbol{\tau}_{ij}^f + \boldsymbol{\tau}_{ij}^d, \quad (3)$$

where $\boldsymbol{\tau}_{ij}^f = \mathbf{p}_{ij} \times {}^SR_i \mathbf{f}_{ij}$ is the torque generated by the force f_{ij} , and $\boldsymbol{\tau}_{ij}^d = {}^SR_i \boldsymbol{\tau}_{ij}$ is the torque generated by the air drag; $\mathbf{p}_{ij} \in \mathbb{R}^3$ is the position of each rotor in $\{S\}$, and SR_i is the orientation of the i -th module in $\{S\}$. Letting $\mathbf{u} = [f_{11}, f_{12}, \dots, f_{n4}]^\top$ be the input vector, we can combine (2) and (3) in a matrix form to define the 6×1 wrench vector

$$\mathbf{w} = \mathbf{A}\mathbf{u}, \quad (4)$$

and the design matrix,

$$\mathbf{A} = \begin{bmatrix} \mathbf{A}_f \\ \mathbf{A}_\tau \end{bmatrix} = \begin{bmatrix} \dots & {}^SR_{ij} \hat{\mathbf{z}} & \dots \\ \dots & \mathbf{p}_{ij} \times {}^SR_{ij} \hat{\mathbf{z}} + {}^SR_{ij} (-1)^{i+j} \frac{k_m}{k_f} \hat{\mathbf{z}} & \dots \end{bmatrix} \quad (5)$$

is a $6 \times 4n$ matrix that maps the input forces into the total wrench in $\{S\}$ which decouples the local force and torque generated by the rotors; and ${}^SR_{ij} = {}^SR_i {}^iR_j$. The design

matrix is also known as the *allocation* matrix [33]. In traditional multi-rotor vehicles, this matrix is fixed after building the robot. In our case, this matrix can change depending on the module configuration.

The dynamics of the structure can be described using the Lagrangian for robot motion [40], [41] as

$$\mathbf{M} \begin{bmatrix} \ddot{\mathbf{r}} \\ \dot{\boldsymbol{\omega}} \end{bmatrix} + \mathbf{C} \begin{bmatrix} \dot{\mathbf{r}} \\ \boldsymbol{\omega} \end{bmatrix} + \mathbf{g} = \mathbf{B}\mathbf{w}, \quad (6)$$

where the matrix $\mathbf{M} = \begin{bmatrix} m\mathbf{I}_3 & \mathbf{0} \\ \mathbf{0} & \mathbf{J} \end{bmatrix}$ collects the mass and inertia tensor of the structure. $\dot{\mathbf{r}}$, $\ddot{\mathbf{r}}$ are the linear velocity and acceleration of the structure; $\boldsymbol{\omega}$, $\dot{\boldsymbol{\omega}}$ are the angular velocity and acceleration of the structure in $\{S\}$, respectively. The matrix $\mathbf{C} = \begin{bmatrix} \mathbf{0} & \mathbf{0} \\ \mathbf{0} & \boldsymbol{\omega} \times \mathbf{J} \end{bmatrix}$ is the Coriolis matrix and $(\cdot)^\times$ operator converts a vector into the corresponding skew-symmetric matrix, $\mathbf{g} = \begin{bmatrix} mg\hat{\mathbf{e}}_3 \\ \mathbf{0} \end{bmatrix}$ is the gravitational force vector, and matrix $\mathbf{B} = \begin{bmatrix} {}^WR_S & \mathbf{0} \\ \mathbf{0} & \mathbf{I}_3 \end{bmatrix}$ maps the wrench vector from the structure's local frame to the world frame. \mathbf{g} is the gravitational acceleration, and \mathbf{I}_3 is the 3×3 identity matrix.

Note that the rank of \mathbf{B} defines along how many generalized coordinates can the multi-rotor generates independent generalized force. For an H-ModQuad structure with dynamics specified as (6), it determines how many entries among $[\ddot{\mathbf{r}}^\top, \dot{\boldsymbol{\omega}}^\top]^\top$ can we control independently, which defines the number of ADOF of the vehicle. Since \mathbf{B} is composed of a rotation matrix and an Identity matrix diagonally, making it always fully ranked, the number of ADOF depends on the rank of the allocation matrix \mathbf{A} . For a quadrotor, the number of ADOF is four [11]. A hexarotor with tilted rotors can have up to six ADOF, defining a fully-actuated robot [17]. We want to design modules with tilted rotors such that they can fly autonomously, and when combined, they can have 4, 5, or 6 ADOF, *i.e.*, achieving full actuation. The configuration in which the modules are combined determines the actuation properties of a structure, such as its ADOF, maximum tilting angle in hover and maximum strength. As the design matrix \mathbf{A} of a structure incorporates the module and rotor configuration information, we would like to model the actuation properties of a structure based on \mathbf{A} . We design a controller for the multi-rotors. The control strategies ought to be generalized such that they work for any structure regardless of its ADOF, number of modules, or their configuration. In this paper, we focus on solving the following problems.

Problem 1 (Module Design). *Given a desired direction of the maximum thrust of a module, specified by the rotation matrix \mathbf{R}^* , find the tilting directions of its rotors, iR_j , such that when all rotors are generating an identical thrust, the total thrust is parallel to the vector $\mathbf{R}^* \hat{\mathbf{z}}$ and the total moment is zero.*

Problem 2 (Modeling Actuation Capabilities). *Given a structure with design matrix \mathbf{A} , develop an analytical model of the its actuation capabilities.*

Problem 3 (Controlling H-ModQuad). *Given a structure with*

either 4, 5 or 6 actuated degrees of freedom, derive a trajectory tracking controller that combines the three cases.

Problem 1, 2, and 3 are discussed in Section IV, V, and VI, respectively.

IV. TORQUE-BALANCED MODULE DESIGN

In order to be able to fly independently, a desirable property for a module that can dock in midair is *torque-balance*. The module can hover without rotating while all rotors generate identical forces.

Definition 3 (torque-balanced module). A torque-balanced module is a module that generates zero torque when all its rotors generate a unit force, i.e., if $\mathbf{u} = \mathbf{1}$, then $\boldsymbol{\tau} = \mathbf{0}$.

In this section, we study the factors to design a *torque-balanced module*.

We reformulate Problem 1 as follows. Given a unit force vector $\hat{\mathbf{f}}^*$, find a combination of ${}^M\mathbf{R}_j$ for the four rotors and an unknown scalar value $\lambda > 0$, such that when all the rotors generate a unit force, i.e., $\mathbf{u} = \mathbf{1}$, the force and torque of the module are

$$\boldsymbol{\tau} = \mathbf{0} \text{ and } \mathbf{f} = \lambda \hat{\mathbf{f}}^*.$$

$\hat{\mathbf{f}}^* = \mathbf{R}^* \hat{\mathbf{z}}$ determines the direction of the thrust force generated by the module in $\{M_i\}$ specified by the rotation matrix \mathbf{R}^* and the magnitude of the desired force, λ . We assume $\lambda > 0$ because $\lambda = 0$ means the module generates zero wrench and thus does not hover when all its rotors are generating identical forces, which does not necessarily indicate uncontrollability, but asymmetry. \mathbf{R}^* is determined during the module design.

Based on (3), the local torque of a module $\boldsymbol{\tau}_i$ depends on thrust $\boldsymbol{\tau}_{ij}^f$, and drag $\boldsymbol{\tau}_{ij}^d$. Typically, the torque created by the force, $\boldsymbol{\tau}_{ij}^f$, is much larger than that by the drag, $\boldsymbol{\tau}_{ij}^d$ because $k_f \gg k_m$. Therefore, a practical solution for $\boldsymbol{\tau}_i = \mathbf{0}$ can be obtained by solving $\sum \boldsymbol{\tau}_{ij}^f = \mathbf{0}$ and $\sum \boldsymbol{\tau}_{ij}^d = \mathbf{0}$ independently. From (2) and (3), we obtain

$$\sum_{j=1}^4 \mathbf{p}_j \times {}^M\mathbf{R}_j \hat{\mathbf{z}} = \mathbf{0}, \quad (7)$$

$$\sum_{j=1}^4 {}^M\mathbf{R}_j (-1)^j \hat{\mathbf{z}} = \mathbf{0}, \quad (8)$$

$$\sum_{j=1}^4 {}^M\mathbf{R}_j \hat{\mathbf{z}} = \lambda \mathbf{R}^* \hat{\mathbf{z}}. \quad (9)$$

Note that the discussion is based on one module, meaning that $n = 1$. For simplicity, we discard the module index i , and \mathbf{p}_j represents the position of the j -th rotor in the module frame. There are two cases for \mathbf{R}^* . In the first case, when $\mathbf{R}^* \neq \mathbf{I}_3$, the *unique* solution that satisfies these constraints is ${}^M\mathbf{R}_j = \mathbf{R}^*$ for all $j = 1, \dots, 4$, ignoring the rotor frames' rotation around their z -axis under the constraint of $\mathbf{R}^* \hat{\mathbf{z}}$ lies in the upper hemisphere of a unit sphere. This leads us to define a specific type of module that creates a sub-group of torque-balanced modules.

Definition 4 (R -module). An R -module is a module that is propelled by a quadrotor, and all its rotors are pointing in the same direction with respect to $\{M\}$, specified by the rotation matrix ${}^M\mathbf{R}_j = \mathbf{R}^*, \forall j = 1, \dots, 4$.

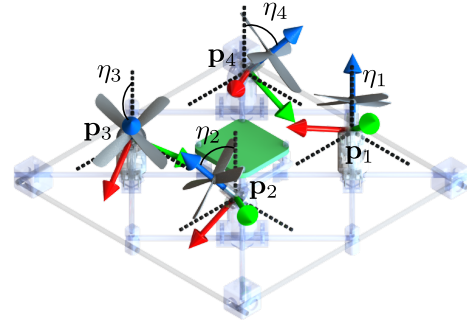


Fig. 4: A T -module where the rotors are tilted around their arms, where the tilting angles $\eta = \eta_1 = -\eta_2 = \eta_3 = -\eta_4$.

Proposition 1. If a module is an R -module, defined by the matrix \mathbf{R}^* as the design factor, the module is a torque-balanced module.

Proof. By definition, ${}^M\mathbf{R}_j = \mathbf{R}^*$. In a quadrotor with a square configuration, the position of the rotors are $\mathbf{p}_1 = -\mathbf{p}_3$ and $\mathbf{p}_2 = -\mathbf{p}_4$. When all rotor forces are identical, i.e., $\mathbf{f}_1 = \mathbf{f}_2 = \mathbf{f}_3 = \mathbf{f}_4$, the torques are cancelled, satisfying (7). The constraints defined in (8) and (9) are satisfied by replacing ${}^M\mathbf{R}_j = \mathbf{R}^*$. In (9), $\lambda = 4$ for any R -module with a non-identity \mathbf{R}^* . \square

In the second case, when $\mathbf{R}^* = \mathbf{I}_3$, the four rotors in the module can point in different directions. Since R -modules maximize the force in a certain direction along which the torque is solely generated from the air drag, we decide to choose a solution such that the module can also have a capability of generating a higher torque along the z -axis of $\{M\}$. Thus, we define a second type of torque-balanced module.

Definition 5 (T -Module). A T -module is a module with its rotors tilted an angle η_j around an axis defined by their arm vector \mathbf{p}_j , $j = 1, \dots, 4$. The angles satisfy $\eta_1 = \eta_3 = -\eta_2 = -\eta_4$. Making $\eta = \eta_1$, we characterize a T -module with a single parameter η .

Proposition 2. If a module is a T -module, defined by the tilting angle η as the design factor, the module is a torque-balanced module.

Proof. By definition of a T -module, the tilted rotors are characterized by the axis-angle representation, where $\hat{\mathbf{p}}_j = \frac{\mathbf{p}_j}{\|\mathbf{p}_j\|}$ is the axis of rotation and η_j is the angle that satisfies $\eta_1 = -\eta_2 = \eta_3 = -\eta_4 = \eta$. We apply Rodrigues' rotation formula to obtain the rotation matrix ${}^M\mathbf{R}_j = \mathbf{I}_3 + (\sin \eta_j) \mathbf{P}_j + (1 - \cos \eta_j) \mathbf{P}_j^2$ from the axis-angle pair $\hat{\mathbf{p}}_j, \eta_j$, where $\mathbf{P}_j = (\hat{\mathbf{p}}_j)^\times$. Since each module has a square configuration, we assume $\mathbf{p}_1 = [a, a, 0]^\top$, $\mathbf{p}_2 = [a, -a, 0]^\top$, $\mathbf{p}_3 = [-a, -a, 0]^\top$, and $\mathbf{p}_4 = [-a, a, 0]^\top$. Replacing ${}^M\mathbf{R}_j$ in terms of η and a , the left hand side of (7) simplifies to $2 \sin \eta (\mathbf{P}_1^2 - \mathbf{P}_2^2) \hat{\mathbf{z}} = \mathbf{0}$. Similarly, we obtain the left hand side of (8), which simplifies to $2(1 - \cos \eta) (\mathbf{P}_2^2 - \mathbf{P}_1^2) \hat{\mathbf{z}} = \mathbf{0}$. Replacing ${}^M\mathbf{R}_j$ in (9) shows $\mathbf{R}^* = \mathbf{I}_3$, and that if and only if ${}^M\mathbf{R}_j = \mathbf{I}_3$ for all $j = 1, \dots, 4$, $\lambda = 4$; otherwise, $\lambda < 4$. \square

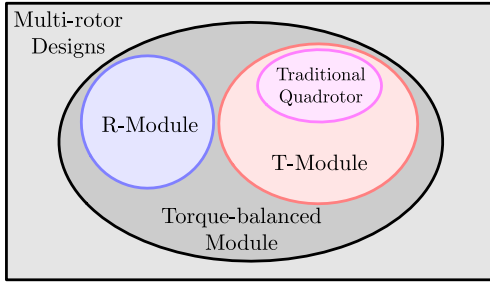


Fig. 5: A Venn diagram showing the relations between R - and T -modules. Traditional quadrotors with all rotors pointing vertically up satisfy criteria of T -modules.

Both R - and T -modules are torque-balanced. Fig. 3 and 4 show the examples of one R - and one T -module, respectively. We show in Fig. 5 a Venn diagram that illustrates the relations between the R - and T -modules. In Table I, we summarize the differences between an R -module and a T -module. A set of modules that include T - and/or R -modules with different design factors is called a *heterogeneous team*. When the heterogeneous team is assembled into a single rigid structure, it forms an *H-ModQuad structure*, or simply a *heterogeneous structure*. In the rest of this paper, a *module* can refer to either a R -module or a T -module, and a *structure* refers to a heterogeneous structure.

V. MODELING ACTUATION CAPABILITIES

Given that the design matrix \mathbf{A} contains all the information regarding the configuration of a structure, including the position and orientation of the rotors in S , our analysis focuses on modeling the actuation capabilities of the structure based on \mathbf{A} . We draw inspiration from the manipulability ellipsoid [42] and force envelope [29], [30], [43], [44] and develop two models that serve different purposes. The first model, the *actuation ellipsoid*, provides an efficient analytical insight into the force capabilities of a structure, but is not capable of incorporating realistic constraints, such as motor saturation or torque constraints. The second model, the *actuation polytope*, involves higher computational complexity but can accommodate constraints to achieve a more accurate and realistic analysis. It also allows designers to evaluate the vehicles against the requirements of aerial tasks.

A. Actuation Ellipsoid

Yoshikawa and Tsuneo [42] introduced the concept of the *manipulability ellipsoid* for robot-arm manipulation by characterizing the response of a manipulator arm based on its design matrix. We extend this concept for multi-rotor vehicles, characterizing the output force in response to the rotor inputs.

TABLE I: Comparison between R - and T -modules

Module	Rotor alignment method	Parameter	Example
R	In the same direction	\mathbf{R}^*	Fig. 3
T	Centrosymmetric around z -axis of $\{M\}$	η	Fig. 4

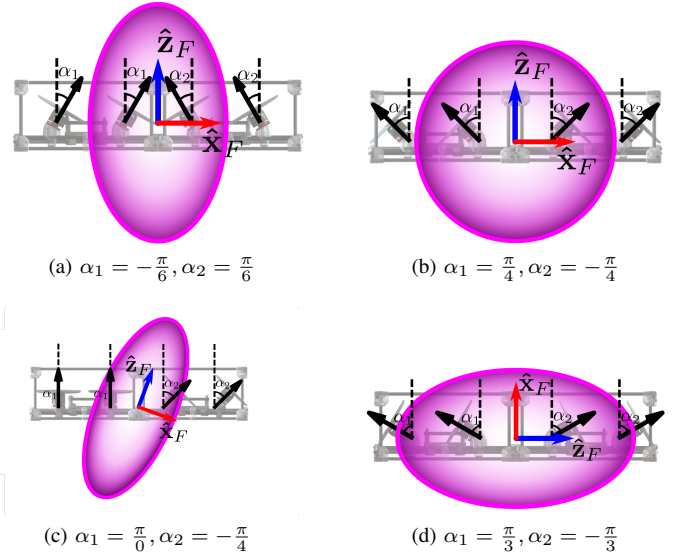


Fig. 6: Side view of four H-ModQuad structures. Each structure consists of two different modules. The black arrows represent the direction of thrust force of the rotors. The purple ellipses represent the projection of the actuation ellipsoid on the xz -plane of $\{S\}$.

The method reveals the direction in which the vehicle is most capable of generating force, with potential application to torque analysis as well.

As shown in (5), \mathbf{A} can be divided into two parts, \mathbf{A}_f and \mathbf{A}_τ which are the first and last three rows of \mathbf{A} , respectively. Note that \mathbf{A}_f maps the input rotor force into the total force in $\{S\}$. We calculate the singular values and singular vectors of the rectangular matrix \mathbf{A}_f by applying singular value decomposition (SVD). Since the singular vectors are orthogonal, we use them to define the semi-axes of the actuation ellipsoid. After normalizing all singular values in the range of $[0, 1]$, we choose the singular vector associated with the largest singular value as the semi-major axis of the actuation ellipsoid, z_F , assuming the center of the ellipsoid is attached at the origin of $\{S\}$. The singular vector associated with the second largest singular value is chosen as the second semi-major axis of the actuation ellipsoid, x_F , and the singular vector associated with the smallest singular value is chosen as the semi-minor axis of the actuation ellipsoid, y_F .

It is possible that the second and third largest singular values are identical after z_F is found. For instance, when $\text{rank}(\mathbf{A}_f) = 1$, all the force vectors from the rotors are co-linear, and the two smallest singular values given by SVD are 0 and z_F is in the direction of the thrust force. In these cases, we set the direction of the second semi-major axis of the actuation ellipsoid closest to the x -axis of $\{S\}$, denoted by \hat{x}_F , i.e., $\mathbf{x}_F = \|\mathbf{x}_F\| \hat{x}_F$, where $\|\mathbf{x}_F\|$ is the magnitude of the singular vector associated with the second largest singular value, and

$$\hat{x}_F = \underset{\mathbf{v}}{\text{argmax}} \mathbf{v} \cdot \hat{x}_S \text{ such that } \|\mathbf{v}\| = 1, \mathbf{v} \cdot z_F = 0,$$

where the first constraint emphasizes that the unit vector \hat{x}_F is the *direction* of the second semi-major axis we choose, and the second constraint ensures the orthogonality of the major and

minor axes of the ellipsoid. Then the semi-minor axis of the ellipsoid is $\mathbf{y}_F = \|\mathbf{y}_F\| \hat{\mathbf{y}}_F$, where $\|\mathbf{y}_F\|$ is the magnitude of the singular vector associated with the smallest singular value and the direction of the semi-minor axis is $\hat{\mathbf{y}}_F = \hat{\mathbf{z}}_F \times \hat{\mathbf{x}}_F$, $\hat{\mathbf{z}}_F = \frac{\mathbf{z}_F}{\|\mathbf{z}_F\|}$.

The actuation ellipsoid intuitively visualizes the structure's capability of generating force in different directions as shown in Fig. 6. We highlight that the higher distance between the boundary of the ellipsoid and the origin of $\{S\}$ means that in the direction the structure can generate force more efficiently. Since the procedure for obtaining the actuation ellipsoid is computationally efficient, we will use this model in Section VI to find the initial robot frame, namely, the F -frame, that the structure can use to maximize hovering efficiency.

B. Actuation Polytope

The actuation ellipsoid of an H-ModQuad vehicle characterizes the capability of the vehicle to generate force in different directions disregarding the constraints on the rotor input itself, such as the uni-directionality of the rotor rotation and the motor saturation, or the torque generation constraints. These constraints limit the actuation capability of H-ModQuad vehicles to meet aerial task requirements. Since most interaction between a multi-rotor vehicle and objects in an environment involves physical contact, we model the requirement of an aerial task for a vehicle as a set of total wrenches that the vehicle needs to generate in $\{S\}$.

Definition 6 (Task Requirement). *A task requirement is a set of wrenches $\mathcal{T} = \{\mathbf{w}_1, \mathbf{w}_2, \dots, \mathbf{w}_t\} \subset \mathbb{R}^6$ that a multi-rotor vehicle needs to generate to perform the task.*

For designers, when assembling a structure for specific tasks, it is essential to ensure that its actuation capability is compatible with the task requirement. Structure evaluation typically involves the construction and testing of prototypes. Although modifying H-ModQuad structures is not overly laborious due to their modularity, testing them can be a tedious process. For this purpose, we develop a method to understand the actuation capability of a structure before it is assembled or evaluated experimentally. We develop the *actuation polytope* as the abstraction of the actuation capability for multi-rotor vehicles composed of unidirectional rotors that have fixed poses with respect to the vehicle. By inspecting the actuation polytope of a vehicle, we are able to understand its actuation capabilities and further reconfigure the modules to achieve better compatibility with a task requirement.

Based on (4) and (5), the design matrix \mathbf{A} converts the rotor force to the total wrench in $\{S\}$. Since the unidirectional rotors can generate a maximum thrust force f_{max} , the set of all possible wrenches that a structure can generate is

$$\mathcal{W} = \{\mathbf{A}\mathbf{u} \mid 0 \preceq \mathbf{u} \preceq f_{max}, \mathbf{u} \in \mathbb{R}^{4n}\}, \quad (10)$$

where “ \preceq ” stands for element-wise comparison and the lower bound 0 captures the unidirectional motor constraint. The constraints on the input vector $0 \preceq \mathbf{u} \preceq f_{max}$ represent the intersection of $2 \cdot 4n$ half-spaces in the \mathbb{R}^{4n} input space, which forms a convex polyhedron [45]. Since the element-wise comparison provides both upper and lower bounds for

the polyhedron along each axis, the polyhedron of constraints is a bounded convex polytope [46]. Mapping such a polytope with an affine function \mathbf{A} to the set of all possible wrenches $\mathcal{W} \subset \mathbb{R}^6$ preserve the convexity and boundedness. Thus, \mathcal{W} is a convex polytope in \mathbb{R}^6 wrench space, which we define as *actuation polytope*.

The definition of the actuation polytope in (10) gives an infinite set in \mathbb{R}^6 , which poses challenges for direct inspection. Since the task requirement \mathcal{T} is defined as a set of required wrenches, we can compare each element in \mathcal{T} with the actuation polytope \mathcal{W} of a structure. Given a required wrench $\mathbf{w}_r \in \mathcal{T} = \lambda_r \hat{\mathbf{w}}$, where λ_r and $\hat{\mathbf{w}}$ are the magnitude and unit vector of \mathbf{w}_r , we can find the maximum magnitude, λ , of the wrench the vehicle can generate in the direction of \mathbf{w}_r by solving the optimization problem

$$\begin{aligned} \max_{\mathbf{u}} \quad & \lambda, \\ \text{subject to} \quad & 0 \preceq \mathbf{u} \preceq f_{max}, \\ & \mathbf{A}\mathbf{u} = \lambda \hat{\mathbf{w}}. \end{aligned} \quad (11)$$

Since $\mathbf{0} \in \mathcal{W}$ always holds true by setting $\mathbf{u} = \mathbf{0}$ and \mathcal{W} is convex, if $\lambda \geq \lambda_r$, then $\mathbf{w}_r \in \mathcal{W}$, meaning that the vehicle is able to satisfy the task requirement \mathbf{w}_r .

Due to the convexity of the actuation polytope, the boundary of \mathcal{W} provides intuitive visualization of the actuation capabilities of a vehicle. By solving (11) for all $\hat{\mathbf{w}}$ that is on a unit 6-sphere, *i.e.*, obtaining the maximum magnitude of the wrenches in \mathcal{W} in all possible directions, we obtain the boundary of \mathcal{W} . By projecting the boundary into the \mathbb{R}^3 force space, we obtain the boundary of the *force envelope* of a structure. Similarly, we can obtain the *torque envelope* by projecting the boundary of \mathcal{W} into the torque space, whose enclosed volume is positively related to the rate at which a structure can twist. However, in reality, the force and torque a structure generates are coupled. For example, when hovering, a structure needs to maintain a constant thrust against gravity, which limits the possible torques it can generate, rendering a fraction of the torque polytope achievable by the structure. To reflect such coupling constraints, Eq. (11) can incorporate additional constraints to reveal actuation properties related to specific tasks. Taking the same example for twisting while hovering without tilting, in need of obtaining the possible torques a fully-actuated structure is able to generate without translating, the designer could constrain the torque polytope with a required force. By adding $\mathbf{A}_f \mathbf{u} = \mathbf{g}$ to the constraints of (11), then projecting the polytope into the \mathbb{R}^3 torque space, the resulted 3-D polytope \mathcal{W}_τ is equivalent to the torque envelope of the structure when the vehicle remains hovering. The structure is capable of generating any torque in the said torque envelope without translation. A *force polytope* can be defined by constraining $\mathbf{A}_\tau \mathbf{u} = \mathbf{0}$ and projecting the polytope into the \mathbb{R}^3 force space, showing how the structure can accelerate linearly without tilting.

The force polytope of a structure is useful to determine the maximum tilting angle while hovering. Since the force polytope is attached to $\{S\}$, the force vector that compensates gravity \mathbf{g} must rotate inside the force polytope depending on the structure's attitude. To verify whether the structure

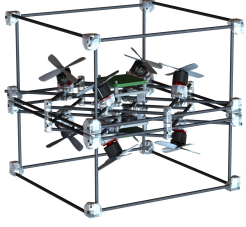
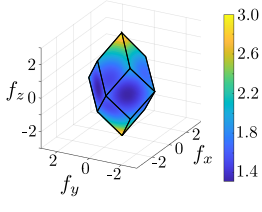
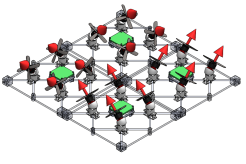
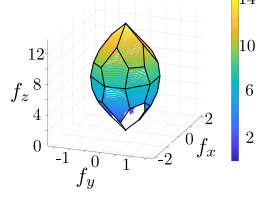
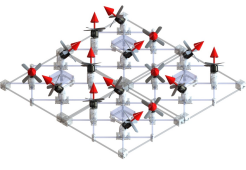
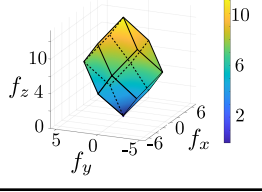
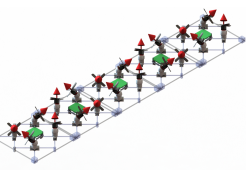
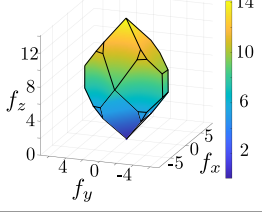
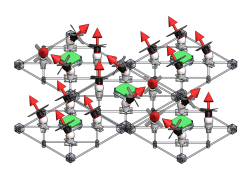
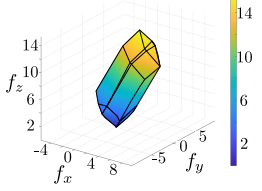
Structure	Force polytope	Structure description	Advantages & disadvantages	Possible applications
		Two T -modules with $\eta_1 = \frac{\pi}{4}$ and $\eta_2 = -\frac{\pi}{4}$ connecting bottom to bottom, creating an omnidirectional structure.	If the magnitude of the gravity force received by the vehicle is less than the shortest distance from the origin to the boundary of the polytope which allows the gravity vector to rotate freely in the polytope, then the vehicle is able to hover at an arbitrary attitude.	<ul style="list-style-type: none"> • Environment 3-D image reconstruction. • Maneuvering in cluttered environment.
		Four R -modules create a 2×2 fully-actuated structure which is used for experiment 3 as shown in Section VII-B3.	The polytope is <i>scaled up along the x- and y-axes by a factor of 4</i> for better visualization. It is tall along z -axis and thin in xy -plane, meaning that the corresponding structure does not allow much tilting but is able to generate more lifting force.	<ul style="list-style-type: none"> • Transporting heavy packages. • Aerial photography. • Base station for coverage control.
		Four T -modules create a 2×2 fully-actuated structure which is used for experiment 4, 5, and 6 as shown in Section VII-B3.	The polytope is wide along xy -plane, meaning that the structure allows a wider range of tilting angles when hovering, but its maximum force is less than that of the second structure.	<ul style="list-style-type: none"> • Transporting delicate objects with attitude constraints.
		Five T -modules compose a 5×1 fully-actuated structure.	The force polytope is wider along the x -axis of $\{S\}$ than that along y -axis, meaning that it is able to generate more force along the x -axis than along y -axis without rotating. Such property makes it easier for the structure to accelerate in one direction.	<ul style="list-style-type: none"> • Navigating through narrow spaces • Drone racing. • Fixed-direction transportation.
		A plus-shape fully actuated structure composed of 3 T -module of 2 types and 2 R -modules which is used for simulation 3.	The leaning z -axis in $\{S\}$ indicates that the structure needs to tilt to achieve the most efficiency in hovering. Such a property allows the structure to efficiently move in cluttered environments where obstacles are mostly in parallel such as a half-collapsed building	<ul style="list-style-type: none"> • Exploring cluttered environment. • Traversal through wind-disturbed fields.

TABLE II: Force polytopes of the corresponding H-ModQuad structures. The second and third structures are the fully-actuated structures used for the real-robot experiments, and the fifth one is the fully actuated structure used in simulation 3.

is capable of achieving a desired attitude ${}^W R_S^d$ while hovering, we calculate the force required to generate in $\{S\}$, $\mathbf{f}^d = \left({}^W R_S^d\right)^\top \mathbf{g}$. This force being the only element in the task requirement, we compare its magnitude $\|\mathbf{f}^d\|$ with the maximum force that the structure can generate in the direction of \mathbf{f}^d by replacing $\hat{\mathbf{w}}$ with $\frac{\mathbf{f}^d}{\|\mathbf{f}^d\|}$, and \mathbf{A} with \mathbf{A}_f in (11). Since hovering requires no rotation, we add another constraint $\mathbf{A}_\tau \mathbf{u} = \mathbf{0}$ in (11). If the maximized force magnitude $\lambda > \|\mathbf{f}^d\|$, then we confirm the structure is able to hover at a desired attitude ${}^W R_S^d$.

Intuitively, structures with their rotors less tilted from the vertical direction have “thinner” force polytopes, which provide the negative gravity vector with a smaller range of rotation while remaining inside the force polytope. Thus, such

structure configurations allow for smaller tilting angles when hovering. In contrast, structures with rotors tilted further from the vertical directions possess “wider” force envelopes that indicate a larger allowed tilt angle when hovering, considering the positive z -axis of $\{S\}$ describes the vertical direction. Applying this method, we obtain that the theoretical maximum tilt angle of the third structure in Table. II is 37.9° in both roll and pitch, and that of the second structure in Table. II is 12° . Both structures are tested in real-robot experiments, which we will compare with our theoretical analysis.

When designing a structure, we primarily examine the force polytope of a structure configuration to determine whether the structure satisfies the intended translation requirements. For example, to enable basic hovering capabilities, a single R - or T -module will satisfy since its force polytope is a line

segment. As long as the magnitude of gravity is less than the length of the line segment, the single-module structure will accomplish the task requirement of hovering. To assemble a fully-actuated structure that is able to generate a large force in one direction, we would like to assemble multiple R -modules with slightly tilted rotors. To design a fully-actuated structure that is able to hover at a large tilting angle, however, we would like to assemble more T -modules with heavily-tilted rotors. In our recent work [47], we have shown how to leverage the actuation polytope to find the optimal configuration of a growing structure given a limited number of homogeneous T -modules. Table II shows some different structure configurations suitable for different tasks. The first row features an omnidirectional structure. The second structure has its force polytope (which is scaled up in x - and y -axes of $\{S\}$ by a factor of 4 for better visualization) thinner than that of the third structure. Although the wider force polytope of the third structure indicates a wider range of tilting at hovering, the maximum weight it can carry is less than that of the second structure, judging from the smaller “height” of the polytope. In the experiments shown in Section VII-B, we verify intuition by discovering that the second structure has a smaller allowed tilting angle along roll and pitch than the third structure.

C. Finding the robot Frame for a Structure

It is possible that the actuation ellipsoid of a structure is practically “invalid”. For example, in Fig. 6(d), the ellipsoid shows that the structure achieves maximum force generation in the horizontal direction. However, considering the unidirectional rotor input constraints, the structure is unable to hover when aligning \hat{z}_F with the negative gravity because it would require two rotors to generate negative forces. In these cases, we can compare the actuation polytope with the ellipsoid to make it more reasonable in practice.

Making it so that x_F, y_F, z_F are collectively decided by the ellipsoid and the polytope. In the \mathbb{R}^3 force space, if $m\mathbf{g}\hat{z}_F \in \mathcal{W}_f$, then the actuation ellipsoid is finalized. Otherwise, it means the structure is unable to hover while keeping \hat{z}_F vertically up. Therefore, we choose the vector in \mathcal{W}_f with the maximum magnitude as the semi-major axis z_F of the actuation ellipsoid, then in the intersection of \mathcal{W}_f and the perpendicular plane of z_F , we choose the vector with the maximum magnitude as the second semi-major axis x_F . Finally, the direction of the semi-minor axis of the ellipsoid is $\hat{y}_F = \hat{z}_F \times \hat{x}_F$, where $\hat{z}_F = \frac{z_F}{\|z_F\|}$ and $\hat{x}_F = \frac{x_F}{\|x_F\|}$. We select the vector on the boundary of \mathcal{W}_f that is in the direction of \hat{y}_F as the semi-minor axis of the ellipsoid.

VI. CONTROL

Our approach for trajectory tracking control is composed of two parts: position and attitude. Fig. 7 shows an overview of the control strategy in a centralized way where all modules in the structure are controlled based on a trajectory function and a single stream of measurements.

Given a desired trajectory function of time, \mathbf{r}^d , a classical trajectory tracking control can compute an acceleration vector

\mathbf{a}_r by deriving the tracking errors, $e_r = \mathbf{r}^d - \mathbf{r}$, and, $e_v = \dot{\mathbf{r}}^d - \dot{\mathbf{r}}$, using the feed-forward equation,

$$\mathbf{a}_r = \mathbf{K}_r e_r + \mathbf{K}_v e_v + g\hat{z} + \ddot{\mathbf{r}}^d, \quad (12)$$

where \mathbf{K}_r and \mathbf{K}_v are diagonal matrices with positive gains.

The maximum total thrust that the structure can generate is not only related to the number of modules but also the orientation of its rotors. In order to utilize the thrust efficiently to achieve the desired acceleration, we introduce the concept of F -frame based on the actuation ellipsoid. We remark that in the direction of the semi-major axis of the ellipsoid, \hat{z}_F , the structure is able to maximize the force generation, and in the direction of the second semi-major axis of the ellipsoid, \hat{x}_F , the structure maximizes its force generation in the normal plane of \hat{z}_F .

Definition 7 (F -frame). *The F -frame of a structure, denoted by $\{F\}$, is a coordinate frame with its origin at the origin of $\{S\}$; the z -axis, \hat{z}_F , points towards the direction where the structure can generate its maximum thrust; the x -axis, \hat{x}_F , points towards the direction where the structure can generate its maximum thrust on the normal plane of \hat{z}_F .*

Therefore, we obtain the rotation matrix from $\{S\}$ to the F -frame, ${}^S\mathbf{R}_F = [\hat{x}_F \ \hat{y}_F \ \hat{z}_F]$, where $\hat{y}_F = \hat{z}_F \times \hat{x}_F$. To maximize the thrust efficiency for different structures, we derive the attitude tracking errors based on the F -frame instead of $\{S\}$.

We compute the attitude error in $SO(3)$ with respect to the F -frame based on [11]. Since the structure has attitude ${}^W\mathbf{R}_F$ and angular velocity ω , the angular tracking error is

$$\begin{aligned} e_R &= \frac{1}{2} \left(\left(({}^W\mathbf{R}_F^d)^\top {}^W\mathbf{R}_S {}^S\mathbf{R}_F - ({}^W\mathbf{R}_S {}^S\mathbf{R}_F)^\top {}^W\mathbf{R}_F^d \right)^\vee \right), \\ e_\omega &= \omega - ({}^W\mathbf{R}_S {}^S\mathbf{R}_F)^\top {}^W\mathbf{R}_F^d \omega^d, \end{aligned} \quad (13)$$

where the “*vee*” operator, \vee , maps a skew symmetric matrix to \mathbb{R}^3 . Note that by design, the readings of the onboard Gyroscope and the external localization system are given with respect to the structure frame, ${}^W\mathbf{R}_S$. In order to maximize the actuation efficiency of the structure, our controllers drive the attitude of $\{F\}$ to the desired attitude ${}^W\mathbf{R}_F^d$. As a result, the attitude of $\{S\}$ converges to ${}^W\mathbf{R}_F^d {}^S\mathbf{R}_F^\top$. Then, the necessary angular acceleration to compensate the attitude error is

$$\mathbf{a}_R = -\mathbf{K}_R e_R - \mathbf{K}_\omega e_\omega, \quad (14)$$

where \mathbf{K}_R and \mathbf{K}_ω are diagonal matrices with positive gains. We highlight that different from the approach proposed by [11], our attitude error is not with respect to the structure frame, $\{S\}$, but the F -frame.

A. Control Policy

Our control policy depends on the rank of \mathbf{A} . We study each case as follows.

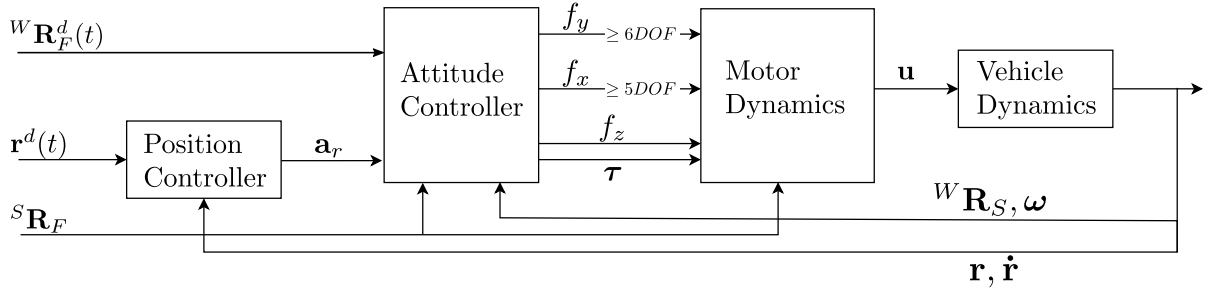


Fig. 7: Control Diagram: We track the desired pose of $\{F\}$, $r^d(t)$, ${}^W\mathbf{R}_F^d(t)$ using the feedback on the pose of the structure frame $\{S\}$, ${}^W\mathbf{R}_S(t)$, $\mathbf{r}(t)$. The Motor Dynamics block is characterized by the matrix $\mathbf{D}\mathbf{A}^\dagger$ depending on the number of ADOF. The rotation matrix from $\{S\}$ to $\{F\}$, ${}^S\mathbf{R}_F$, is computed based on the structure configuration.

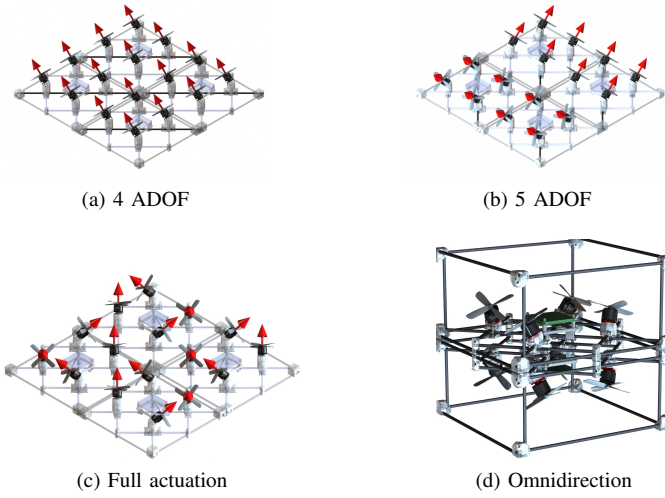


Fig. 8: Four possible H-ModQuad configurations. In (a), the vehicle is composed of four identical R -modules pointing in the same direction, and thus has 4 ADOF. In (b), the vehicle is composed of four R -modules, two pointing in one same direction and the other two pointing in another, thus has 5 ADOF. In (c), the vehicle is composed of four T -modules and has 6 ADOF, *i.e.*, fully-actuated. In (d), the vehicle is composed of two T -modules assembled back to back and is omnidirectional based on the definition given by [32].

1) *4 ADOF*: For a structure with $\text{rank}(\mathbf{A}) = 4$, as shown in Fig. 8(a), similar to a traditional quadrotor, we can control the position and yaw angle of the structure using a geometric controller [11]. However, different from the procedures by [11], we project the desired thrust vector on the z -axis of $\{F\}$, instead of $\{S\}$. This approach reduces the energy consumption since the reference force is in the direction of the maximum force of the structure. Given a desired acceleration vector \mathbf{a}_r and a desired yaw angle ψ^d , the desired attitude ${}^W\mathbf{R}_F^d = [\hat{\mathbf{x}}^d \hat{\mathbf{y}}^d \hat{\mathbf{z}}^d]$ of the structure is obtained by

$$\begin{aligned} \hat{\mathbf{z}}^d &= \frac{\mathbf{a}_r}{\|\mathbf{a}_r\|}, & \hat{\mathbf{x}}^c &= [\cos(\psi^d), \sin(\psi^d), 0]^\top \\ \hat{\mathbf{y}}^d &= \frac{\hat{\mathbf{z}}^d \times \hat{\mathbf{x}}^c}{\|\hat{\mathbf{z}}^d \times \hat{\mathbf{x}}^c\|}, & \hat{\mathbf{x}}^d &= \hat{\mathbf{y}}^d \times \hat{\mathbf{z}}^d. \end{aligned} \quad (15)$$

2) *5 ADOF*: For a structure with at least two modules and $\text{rank}(\mathbf{A})=5$, as shown in Fig. 8(b), the vehicle gains actuation over one additional ADOF. Since the second semi-major axis of $\{F\}$ is $\hat{\mathbf{x}}_F$, meaning that the structure is able to generate forces in $\hat{\mathbf{x}}_F$ independently, the additional ADOF is given to the rotation around $\hat{\mathbf{y}}_F$. We choose to use this additional DOF to track the pitch angle of $\{F\}$, θ^d . The desired attitude, ${}^W\mathbf{R}_F^d = [\hat{\mathbf{x}}^d \hat{\mathbf{y}}^d \hat{\mathbf{z}}^d]$ of the structure is obtained by

$$\begin{aligned} \hat{\mathbf{z}}^c &= \frac{\mathbf{a}_r}{\|\mathbf{a}_r\|}, & \hat{\mathbf{x}}^d &= \text{Rot}(z, \psi^d) \text{Rot}(y, \theta^d) \hat{\mathbf{x}}, \\ \hat{\mathbf{y}}^d &= \frac{\hat{\mathbf{z}}^c \times \hat{\mathbf{x}}^d}{\|\hat{\mathbf{z}}^c \times \hat{\mathbf{x}}^d\|}, & \hat{\mathbf{z}}^d &= \hat{\mathbf{x}}^d \times \hat{\mathbf{y}}^d, \end{aligned} \quad (16)$$

where the operators $\text{Rot}(x, \cdot)$, $\text{Rot}(y, \cdot)$, and $\text{Rot}(z, \cdot)$ convert the Euler angles in roll, pitch, and yaw into rotation matrices, respectively. Different from (15), in (16), instead of projecting $\hat{\mathbf{x}}^c$ on the normal direction of the $\hat{\mathbf{y}}^d \hat{\mathbf{z}}^d$ -plane to obtain $\hat{\mathbf{x}}^d$, we obtain $\hat{\mathbf{x}}^d$ directly by applying the desired yaw and pitch angle on $\hat{\mathbf{x}}$. $\hat{\mathbf{z}}^c$ is projected on the normal direction of the $\hat{\mathbf{x}}^d \hat{\mathbf{y}}^d$ -plane to acquire the desired force in the xz -plane of $\{F\}$, in which all possible forces that the structure can generate are co-planar. This method makes sure the desired attitude captures the desired pitch angle.

3) *6 ADOF*: For a structure with $\text{rank}(\mathbf{A})=6$, as shown in Fig. 8(c) and (d), the vehicle is fully actuated. Therefore, the desired attitude ${}^W\mathbf{R}_F^d$ is chosen independent from the desired position.

Substituting ${}^W\mathbf{R}_F^d$ in (13) and then plugging in the errors to (14), we obtain the desired angular acceleration \mathbf{a}_R . Combining \mathbf{a}_R with the desired positional acceleration vector \mathbf{a}_r , we generate an acceleration vector $\mathbf{a} = [\mathbf{a}_r^\top, \mathbf{a}_R^\top]^\top$. Based on (6), to implement feedback linearization, we let the structure to generate wrench \mathbf{w} in $\{F\}$

$$\mathbf{w} = \begin{bmatrix} {}^W\mathbf{R}_F^\top & \mathbf{0} \\ \mathbf{0} & \mathbf{J} \end{bmatrix} \left(\mathbf{a} + \begin{bmatrix} \mathbf{0} \\ \boldsymbol{\omega} \times \mathbf{J}\boldsymbol{\omega} \end{bmatrix} \right). \quad (17)$$

When \mathbf{A} is full-row rank, based on (4), we can calculate the desired input vector using Moore-Penrose inverse, or pseudo-inverse, $\mathbf{u} = \mathbf{A}^\dagger \mathbf{w}$, which minimizes the square sum of the rotor thrusts. The result of this method can require negative entries for \mathbf{u} , which is unachievable by uni-directional motors.

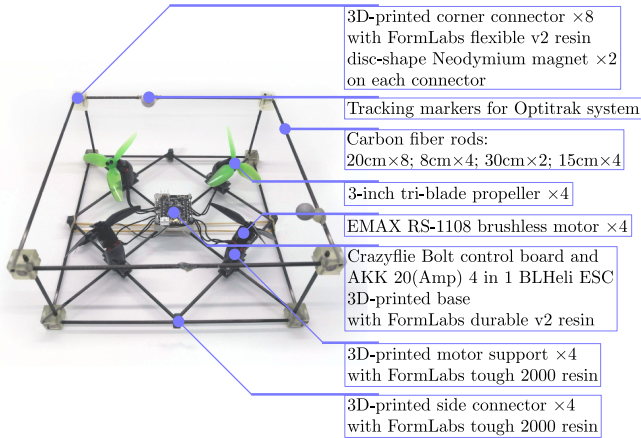


Fig. 9: A T -module prototype with $\eta = \frac{\pi}{4}$. The main components are labelled.

When \mathbf{A} is not full-row rank, we cannot apply pseudo inverse on it directly. In a general form, we introduce the *Dimensioning matrix* \mathbf{D} , such that (4) changes into

$$\mathbf{D}\mathbf{w} = \mathbf{D}\mathbf{A}\mathbf{u},$$

for

$$\mathbf{D} = \begin{cases} \begin{bmatrix} \mathbf{0}_{4 \times 2} & \mathbf{I}_4 \end{bmatrix}, & \text{rank}(\mathbf{A}) = 4, \\ \begin{bmatrix} \begin{bmatrix} 1 & 0 \end{bmatrix} & \mathbf{0}_{1 \times 4} \\ \mathbf{0}_{4 \times 2} & \mathbf{I}_4 \end{bmatrix}, & \text{rank}(\mathbf{A}) = 5, \\ \mathbf{I}_6, & \text{rank}(\mathbf{A}) = 6, \end{cases} \quad (18)$$

where $\mathbf{I}_a \in \mathbb{R}^{a \times a}$ stands for an $a \times a$ identity matrix, and $\mathbf{0}_{a \times b} \in \mathbb{R}^{a \times b}$ represents a zero matrix of size $a \times b$. We can then calculate the desired input vector by applying Moore-Penrose inverse on matrix $\mathbf{D}\mathbf{A}$,

$$\mathbf{u} = (\mathbf{D}\mathbf{A})^\dagger \mathbf{D}\mathbf{w}, \quad (19)$$

which is referred to as the ‘‘Motor Dynamics’’ in Fig. 7, where the input of the i -th module,

$$\mathbf{u}_i = (\mathbf{D}\mathbf{A})_i^\dagger \mathbf{D}\mathbf{w}, \quad (20)$$

where $i = 1, \dots, n$, and $(\mathbf{D}\mathbf{A})_i^\dagger$ is the submatrix of $(\mathbf{D}\mathbf{A})^\dagger$ composed of its $(4i - 3)$ -th to $4i$ -th rows.

The controller is exponentially stable and its proof follows the same logic as that presented by [11] but using ${}^W\mathbf{R}_F$ instead of ${}^W\mathbf{R}_S$.

VII. EVALUATION

We use experiments and simulations to evaluate the modular multi-rotor design and our methods. The experiments validate the control strategies with actual robots, and the simulations illustrate the scalability of H-ModQuad. We design six different experiments and three simulations.

A. H-ModQuad robots

1) *Design*: We build the H-ModQuad modules based on the Crazyflie framework. Since the original Crazyflie 2.1 drone has a low payload (< 10 g), we design a quadrotor module with brushless motors and the Crazyflie Bolt control board. The design for traditional quadrotors and R -modules were previously validated by [25], [48]. We show a prototype of our new T -module design in Fig. 9. Each module weighs 135 g, including a 2-cell LiPo battery. It has a payload capability of 128 g.¹

The docking mechanism for self-assembly is based on permanent magnets on the 3D-printed corners of the module frame as shown in Fig. 9. The disc-shape Neodymium magnets can create rigid connection between a pair of modules. Each magnet has a radius of 3.15 mm and a thickness of 1.5 mm. Its weight is negligible. Since such a in-flight docking mechanism was validated in [14], the experiments will assume the docking is accomplished, and we focus on the behaviors of the structures as an entirety.

In the experimental testbed, we use the Crazyflie-ROS framework [49] to command the robots. In order to incorporate our controller, we modified the Crazyflie firmware.² For the localization of the quadrotors, we use the motion capture system (Optitrak) operating at 120 Hz. The Crazyflie Bolt internally measures the angular velocities and linear accelerations using the IMU. The readings from the sensors and tracking systems are combined with an on-board extended Kalman filter [50], [51]. Autonomous docking was presented in [14]. In the experiments of this work, we focus on evaluating the new module design, the effectiveness of the proposed analysis, and the performance of the control strategy during flight. Therefore, the vehicles are manually assembled.

2) *Localization and Communication*: In the experiments, all modules of a structure and the structure compose their own rigid bodies in the Optitrak localization system. The Optitrak system broadcasts the pose of the structure rigid body. Based on the received pose, the Crazyflie-ROS framework updates the position and attitude directly on the Kalman filter running on each module since we consider the structure a rigid body. The onboard Kalman filter fuses the received Optitrak pose with the readings from the onboard IMUs such as the accelerometer and the gyroscope to generate a local state estimation.

The central station broadcasts commands in the form of desired states composed of position, orientation, linear and angular velocity. Upon reception of the commands, all modules run the position and attitude controller independently based on their own state estimation. Across different modules, their knowledge of the inverse dynamics shown as the motor dynamics block in Fig. 7 is unique for each individual module. This difference is related to the relative position and orienta-

¹A complete list of components and assembly instruction can be found at <https://docs-quad.readthedocs.io/en/latest/assemble/design.html>

²The source code for the actual robots is available on GitHub: the modified Crazyflie-ROS framework is on https://github.com/swarmslab/customized_Crazyflie_ros and the modified firmware of Crazyflie is on <https://github.com/swarmslab/modquad-firmware/tree/HModQuad> for the 2×2 structure in experiment 4, 5, and 6.

tion of the modules to the structure frame, and is implemented onboard, allowing the modules to independently determine the inputs to its rotors so that the structure can generate the desired wrench. In the experiment, we hardcode the corresponding motor dynamics for each module. In simulation, we let the modules sense their own pose with regard to $\{S\}$, and compute the power distribution. There is no inter-module communication implemented.

B. Experiments

In Experiments 1, 2, and 3, we validate our method on structures composed of R -modules. In Experiments 4, 5, and 6, we show the performance of the fully actuated structure composed of T -modules.

1) *Experiment 1 - One R-module, 4DOF helix* : In our first experiment, we validate our controller by testing a structure that has an F -frame that is not aligned with $\{S\}$. A single R -module forms such a structure, with all its rotors tilting 10 degrees along pitch. Thus, the structure of one module has the F -frame specified by ${}^S\mathbf{R}_F = \text{Rot}(y, \frac{\pi}{18})$. The task for this structure is to track a 4-DOF trajectory (position and yaw orientation). We design a vertical-helix trajectory in $\{W\}$ for the structure to move along. The helix centers at $(-0.5, 0)$ in the xy -plane with a radius of 0.45 m and oscillates along the z -axis between 0.45 m and 0.95 m with a period of 14 seconds. While tracking the position, the structure is also rotating the yaw angle with a period of 18 seconds. The experiment result is shown in Fig. 10. The average error in position is $\mu_x = 0.0043$ m, $\mu_y = -0.0045$ m, and $\mu_z = 0.0098$ m, and its standard deviations $\sigma_x = 0.0398$ m, $\sigma_y = 0.0423$ m, $\sigma_z = 0.0437$ m. The errors in angle is $\mu_\psi = -0.4131^\circ$, and their standard deviation $\sigma_\psi = 3.6729^\circ$. The average errors in the x -, y -, and z -axes are under 0.05 m, and the error in yaw is under 1.0° . We highlight that the structure of one module has an attitude ${}^W\mathbf{R}_S = {}^S\mathbf{R}_F^\top$ during hovering, showing that we are driving the F -frame to track the desired attitude.

2) *Experiment 2 - Rectangle tracking* : In the second experiment, we validate our control strategy and the *dimensioning matrix* by testing a structure with 5 ADOF, composed of two R -modules. The structure tracks a rectangular trajectory on the xy -plane of $\{W\}$ with a length of 0.8 m and a width of 0.6 m. One module has all its rotors tilting 30 degrees in pitch and the other tilting -30 degrees in pitch, which resulted in a design matrix \mathbf{A} whose $\text{rank}(\mathbf{A}) = 5$. The resulted F -frame aligns with $\{S\}$, thus ${}^S\mathbf{R}_F$ is a 3×3 identity matrix. The structure can track the rectangle trajectory when its $\{S\}$ has a pitch angle of 0 and -5 degrees, which illustrates the independence of its translation on the x -axis and its pitch

Exp.	R -modules	T -modules	#ADOF	Trajectory
1	1	0	4	Helix
2	2	0	5	Rectangle
3	4	0	6	Rectangle
4	0	4	6	$\sin(t)$ for ϕ
5	0	4	6	Input ϕ
6	0	4	6	Rectangle

TABLE III: Module types, number of ADOF and trajectory types of the six experiments.

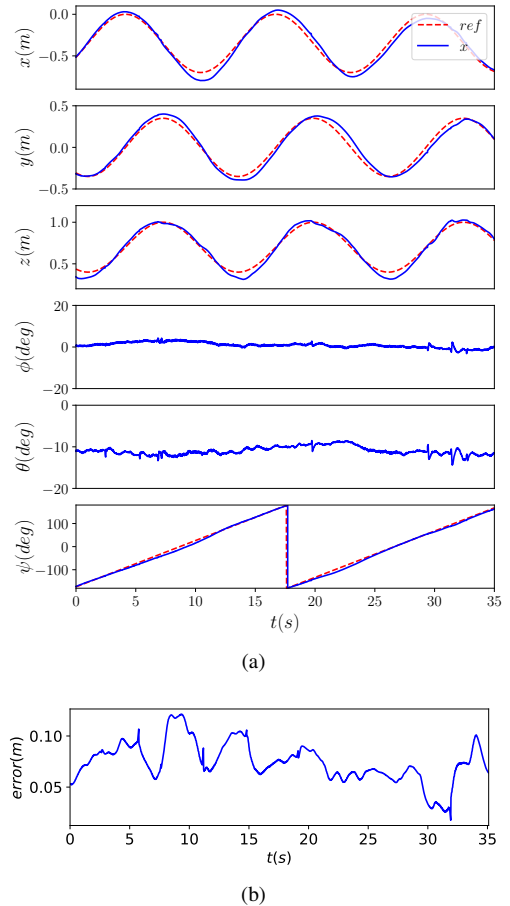


Fig. 10: Experiment 1: a) A structure with 4 ADOF following a 4-DOF trajectory. b) Euclidean distance between the desired and the actual position.

angle. The result is shown in Fig. 11. The average error in position is $\mu_x = -0.0818$ m, $\mu_y = -0.0059$ m, and $\mu_z = 0.0055$ m, and its standard deviations $\sigma_x = 0.1227$ m, $\sigma_y = 0.0979$ m, $\sigma_z = 0.0322$ m. The angle errors are $\mu_\phi = 1.7718^\circ$, $\mu_\theta = 1.3353^\circ$, $\mu_\psi = 0.7125^\circ$, and their standard deviation $\sigma_\phi = 1.2356^\circ$, $\sigma_\theta = 0.6866^\circ$, and $\sigma_\psi = 1.4248^\circ$.

The structure has the largest error along the x -axis despite the reference pitch angle, where the error is below 0.09 m. Along the y - and z -axes, the structure keeps the error less than 0.06 m. We highlight when the structure is pitching -5.0 degrees and moving in the positive x -direction, it is moving in the opposite direction to where the structure can generate its maximum thrust.

3) *Experiment 3 - Rectangle tracking* : In the third experiment, we validate our control strategy for a fully-actuated structure. Our structure is composed of four R -modules to track a 0.8×0.6 rectangular trajectory on the xy -plane of $\{W\}$ without any tilting. We assemble the modules in the structure as a 2×2 square in the xy -plane of $\{S\}$. We label the module in the second, third, fourth, and first quadrant of the xy -plane of $\{S\}$ as module 1, 2, 3, and 4. In module 1, 3, 2, and 4, the rotors are tilting 30, -30 degrees in pitch, -30, and 30 degrees in roll, respectively. Thus, ${}^S\mathbf{R}_{M_1} = {}^S\mathbf{R}_{M_3}^\top = \text{Rot}(y, \frac{\pi}{6})$ and ${}^S\mathbf{R}_{M_2} = {}^S\mathbf{R}_{M_4}^\top = \text{Rot}(x, -\frac{\pi}{6})$. The F -frame aligns with

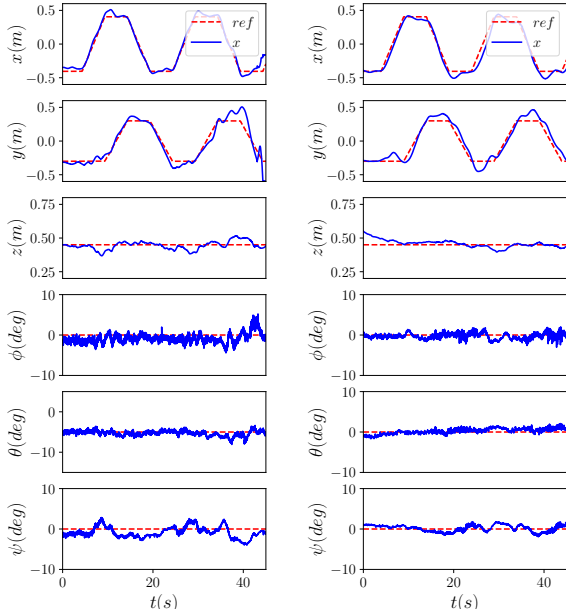
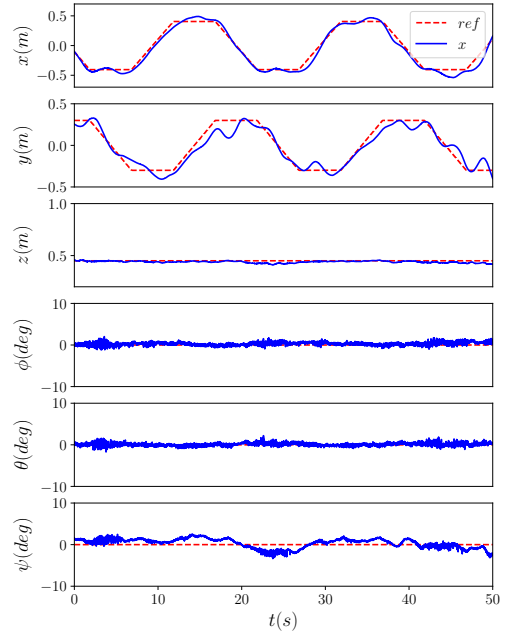


Fig. 11: Experiment 2: An H-ModQuad structure of two modules track a rectangle with two *different* fixed pitch angles. The plot on the left shows the structure following the rectangle while keeping a pitch angle of -5 degrees; on the right shows the structure tracking the rectangle while keeping a pitch angle of 0 degrees.

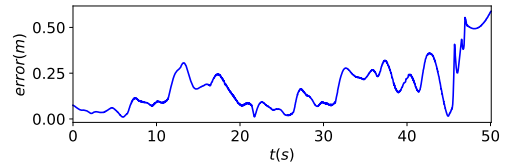
$\{S\}$, making ${}^S\mathbf{R}_F$ a 3×3 identity matrix. The experiment result is shown in Fig. 12. The average error in position is $\mu_x = 0.0039$ m, $\mu_y = -0.0028$ m, and $\mu_z = 0.0207$ m, and its standard deviations $\sigma_x = 0.0898$ m, $\sigma_y = 0.0783$ m, $\sigma_z = 0.0158$ m. The errors in angle is $\mu_\phi = 0.0609^\circ$, $\mu_\theta = 0.0306^\circ$, $\mu_\psi = 0.1411^\circ$, and their standard deviation $\sigma_\phi = 0.4735^\circ$, $\sigma_\theta = 0.3255^\circ$, and $\sigma_\psi = 0.6361^\circ$.

Along the y -axis, the structure has largest error, but below 0.15 m. Along the x - and z -axes, the structure keeps the error under 0.05 m. We highlight that when the structure is tracking the rectangle trajectory, both its roll and pitch angles stay at 0 degrees, which shows the independence of translation and orientation.

4) *Experiment 4 - sinusoidal roll* : We notice that the H-ModQuad configuration in Experiment VII-B3 has very limited capability in tilting without translating due to the uni-directional motor constraints. Therefore, in the fourth experiment, we assemble a structure composed of four T -modules, showing that the structure of 6 ADOF is able to tilt without translation. The four T -modules are of two types, one with $\eta = \frac{\pi}{4}$, and the other with $\eta = -\frac{\pi}{4}$. The two types of T -modules are placed diagonally as a 2×2 square in the xy -plane of $\{S\}$, as shown in Fig. 8 (c), making ${}^S\mathbf{R}_F$ a 3×3 identity matrix. The task for the structure in this experiment is to track a sinusoidal curve in pitch angle while hovering in place. The reference sinusoidal curve has a period of 90 seconds and has a magnitude of 20 degrees. While continuously tilting, the structure is generating independently controllable force and torque at the same time. Because the



(a)



(b)

Fig. 12: Experiment 3: a) A fully-actuated structure of 4 R -modules following a rectangular shape without tilting. b) Euclidean distance between the desired and the actual position.

structure is centrosymmetric, the capability of tilting along roll and pitch are equivalent. The experiment result is shown in Fig. 13. The average error in position is $\mu_x = -0.0104$ m, $\mu_y = -0.0143$ m, and $\mu_z = -0.0555$ m, and its standard deviations $\sigma_x = 0.2453$ m, $\sigma_y = 0.0687$ m, $\sigma_z = 0.1318$ m. The angle errors are $\mu_\phi = -0.3988^\circ$, $\mu_\theta = -0.6541^\circ$, $\mu_\psi = 0.3093^\circ$, and their standard deviation $\sigma_\phi = 1.8583^\circ$, $\sigma_\theta = 2.435^\circ$, and $\sigma_\psi = 1.019^\circ$.

Along the x - and z -axes, the structure keeps the error under 0.06 m. Along all three axes, the structure keeps the error in rotation under 3.0° . We highlight that the structure is able to change its roll angle while maintaining hover in place. The position error is mainly caused by the mismatch from the crafting against the *Motor Dynamics* model of the structure, which is compensated by the feedback controller.

5) *Experiment 5 - Manual roll* : We observe in Experiment VII-B4 that the H-ModQuad in Fig. 8(c) has a better capability in tilting than the one of four R -modules in Experiment VII-B3. In order to find the maximum tilting angle of this configuration with four T -modules, we design another experiment to manually increase the reference roll angle until the structure is unable to remain hovering in place while tracking the tilting angle. The experiment result is shown in Fig. 14. We observe that as the reference tilting angle increases, some

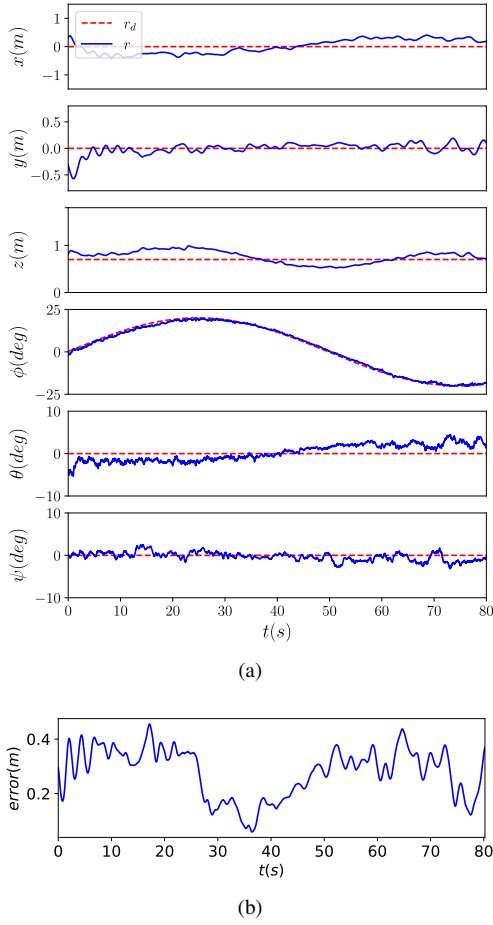


Fig. 13: Experiment 4: a) A fully-actuated structure of 4 T -modules tilting in roll without translation. b) Euclidean distance between the desired and the actual position.

rotors stops rotating as a result of *Motor Dynamics*, as shown in Fig. 1. According to [52], when the commanded rotor force is below a threshold, the linear relation between the generated force and the PWM no longer holds, which causes the mismatch between the deployed model and the physical system of the H-ModQuad. The average error in position is $\mu_x = 0.3389$ m, $\mu_y = 0.0309$ m, and $\mu_z = -0.3451$ m, and its standard deviations $\sigma_x = 0.1898$ m, $\sigma_y = 0.0941$ m, $\sigma_z = 0.1659$ m. The angle errors are $\mu_\phi = 1.5495^\circ$, $\mu_\theta = 0.3805^\circ$, $\mu_\psi = -0.2988^\circ$, and their standard deviation $\sigma_\phi = 1.1736^\circ$, $\sigma_\theta = 0.971^\circ$, and $\sigma_\psi = 1.2678^\circ$.

Along the y -axis, the error is below 0.05 m; along the z -axis, the error goes up to 0.5 m; along the x -axis, the error reaches 0.8 m when the structure is approaching the maximum tilting angle in roll. Based on this experiment, the robot can achieve a maximum roll angle of 38.0° , which is consistent with the results given by the actuation polytope analysis.

6) *Experiment 6 - Rectangle tracking* : In this experiment, we have a similar task as Experiment VII-B3 but using an H-ModQuad structure composed of T -modules. The experiment result is shown in Fig. 15. The average error in position is $\mu_x = 0.0039$ m, $\mu_y = -0.0028$ m, and $\mu_z = 0.0207$ m, and its standard deviations $\sigma_x = 0.0898$ m, $\sigma_y = 0.0783$ m, $\sigma_z =$

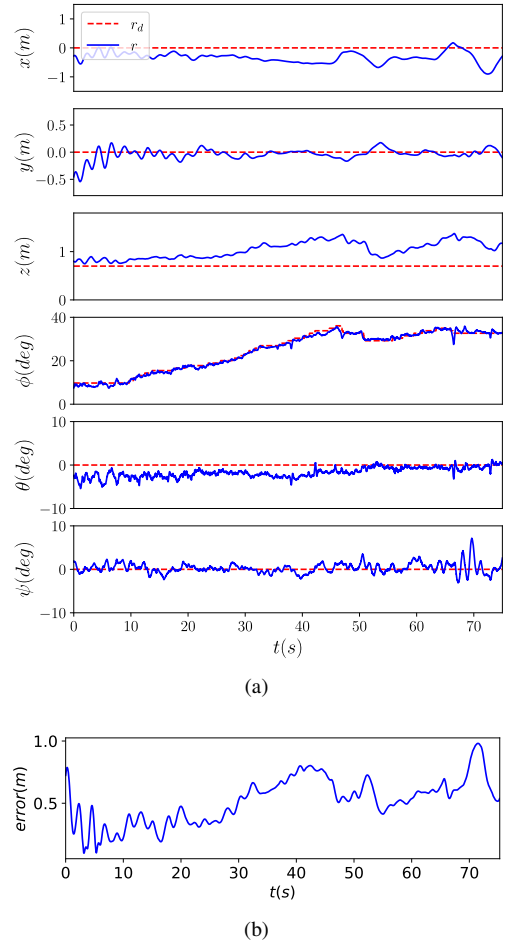


Fig. 14: Experiment 5: a) A fully-actuated structure of 4 T -modules reaching maximum-possible tilting in roll. b) Euclidean distance between the desired and the actual position.

0.0158 m. The angle errors are $\mu_\phi = 0.0609^\circ$, $\mu_\theta = 0.0306^\circ$, $\mu_\psi = 0.1411^\circ$, and their standard deviation $\sigma_\phi = 0.4735^\circ$, $\sigma_\theta = 0.3255^\circ$, and $\sigma_\psi = 0.6361^\circ$.

The positional error is below 0.04 m along all axes, and the rotational error is below 0.5 degrees along all axes. Combining Experiment VII-B4 and VII-B6, we show in full that this H-ModQuad of 4 T -modules is fully actuated and has control over all its 6 DOF in motion.

C. Simulation

The experiments show that the control strategy for H-ModQuad structures work for different configurations using real-world prototypes with 4, 5, and 6 ADOF. In our simulations, we test aspects of the H-ModQuad design that may induce challenges due to limited resources and safety concerns in real-robot experiments such as the scalability and the controller robustness against realistic constraints. With access to more modules and more complex configurations, we implement three tests in the simulation.³

³The source code for the simulations is available on GitHub: <https://github.com/swarmslab/HModQuad-sim>

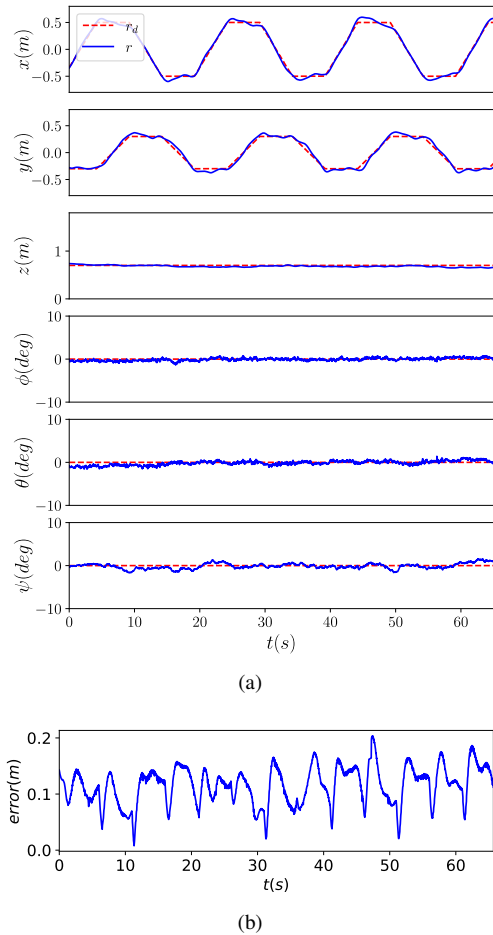


Fig. 15: Experiment 6: a) A fully-actuated structure of 4 T -modules following a rectangular shape without tilting. b) Euclidean distance between the desired and the actual position.

We choose to test the structures in CoppeliaSim simulation environment [53] with Python API. We match the dimensions and weights of the structures to our prototypes. The structures for all three simulations are fully-actuated and their task is to follow a Quintic-polynomial trajectory of 6 DOF [12], [54]. Fig. 16 (a), (b), and (c) show the three structures in the simulation environment. Simulation 1 tests the controller robustness with a large structure in which the non-rigid connections between modules may lead to misalignment of modules and the resulted deformation of the structure. Simulation 2 and 3 assume rigid connections between modules so that the structure acts as a monolithic rigid body. Simulation 2 and 3 involve structures composed of different types of T - and R -modules. Specifically, simulation 3 provides a non-trivial example of a structure not having its F -frame aligned with $\{S\}$.

1) *Simulation 1*: In this simulation, we assemble a 4×4 H-ModQuad structure with 16 T -modules that is a two-time scaled-up equivalence of the structure used in Experiment VII-B4 and VII-B5, and VII-B6. Different from the later simulations, the structure is composed of linked modules instead of being a monolithic rigid body. These links between modules lead to possible relative displacement, making the

structure deform during a flight. The simulation result is shown in Fig. 17. The position tracking has an error under 0.02 m along the x -, y -, and z -axes. The attitude keeps the error under 5.0 degrees in pitch and roll, and under 1.0 degrees in yaw. Notably, although the non-rigidity of the structure is causing the noise in roll and pitch stabilization, the structure is still able to follow the trajectory.

2) *Simulation 2*: In this simulation, we want to show the versatility of the modular system by assembling different types of torque-balanced modules. We construct a 3×3 H-ModQuad structure of five types of torque-balanced modules. Five out of the nine modules are T -modules of the same type with $\eta = \frac{\pi}{4}$, and they are placed at the four corners and the center of the 3×3 structure. The other modules are the same four R -modules we used in Experiment 3. They are placed on the four sides of the 3 structure with all their rotors tilting 30 degrees towards the center of the structure. In practice, R -modules are better for translation and T -modules are better for rotation. A structure with both T - and R -modules, such as the one we construct for this simulation, can complete tasks that involve both linear and rotational motions. Fig. 18 shows the simulation result of this H-ModQuad structure. The error in position is under 0.02 m along all axes. The attitude tracking error is under 3.0 degrees in pitch and roll, and under 1.0 degrees in yaw.

3) *Simulation 3*: To show the effectiveness of the method of Actuation Ellipsoid, we construct a fully-actuated “plus”-shape structures with 1 T -module of $\eta = -\frac{\pi}{4}$ in the center, 2 T -modules of $\eta = \frac{\pi}{4}$ on two opposite wings and 2 R -modules tilting in the same direction on the other two wings. The rotors of the R -modules tilt $\frac{\pi}{4}$ radians in the positive y -direction of their module frame. The resulted F -frame has a 23-degree leading mismatch in pitch with $\{S\}$. As shown in Fig. 19, when following the trajectory, the pitch error of $\{S\}$ is around 20-degree and the attitude error based on the F -frame is close to 0, showing that the structure is actuating to align its F -frame with the reference while the positional error is maintained below 0.05 meters.

D. Discussion

We discuss on some observations and challenges during the evaluation. The R -modules in Experiment 1-3 show that the generalized controller applies effectively on the cases where the multi-rotor structure has 4, 5, and 6 ADOF. We note that while having six ADOF as we assemble four R -modules together, the structure used in Experiment 3 experiences the issue of losing stability as some of the motors reach its maximum thrusting force, especially when the structure is tracking a large tilting angle along roll or pitch. The observation matches our intuition from the “thin” force polytope on the fully-actuated structure composed of only R -modules. Moreover, the calculated maximum tilting angle of the structure based on the force polytope being 12° also infers that the theoretical maximum force it can generate in the horizontal plane of the F -frame is less than $\tan 12^\circ \approx 0.21$ times that in the z -axis, significantly limiting the trajectory tracking capabilities of the structure in horizontal translation.

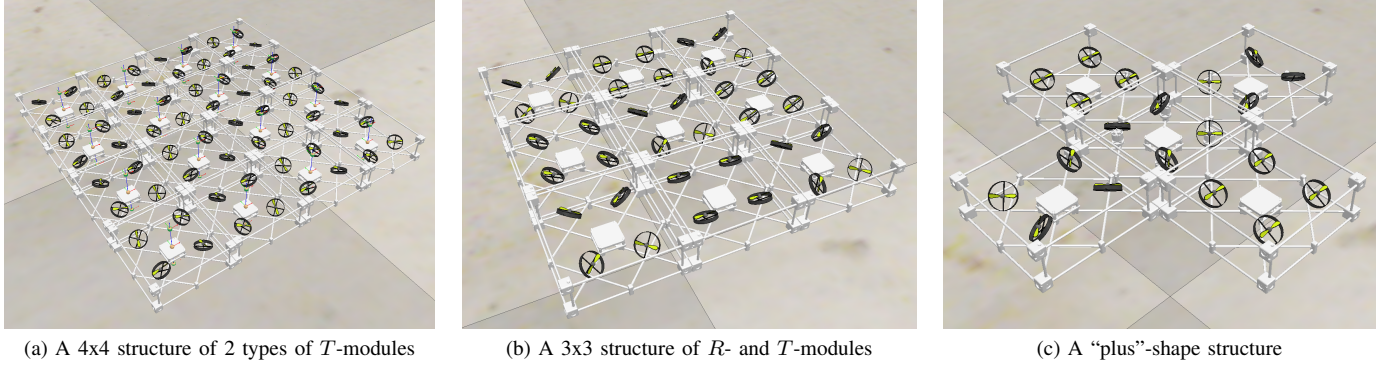
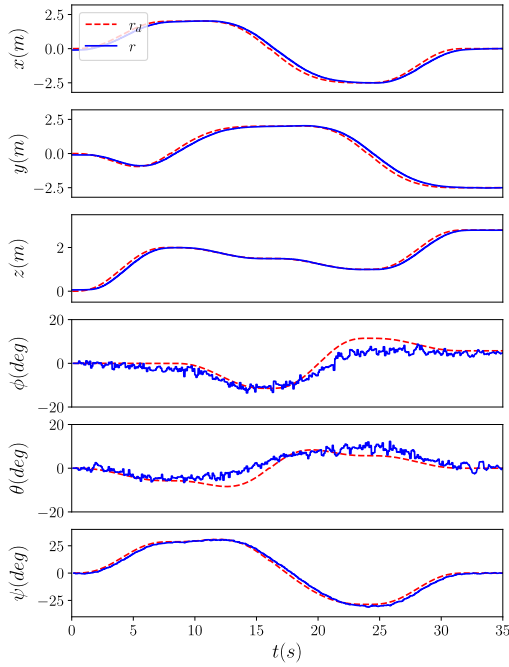
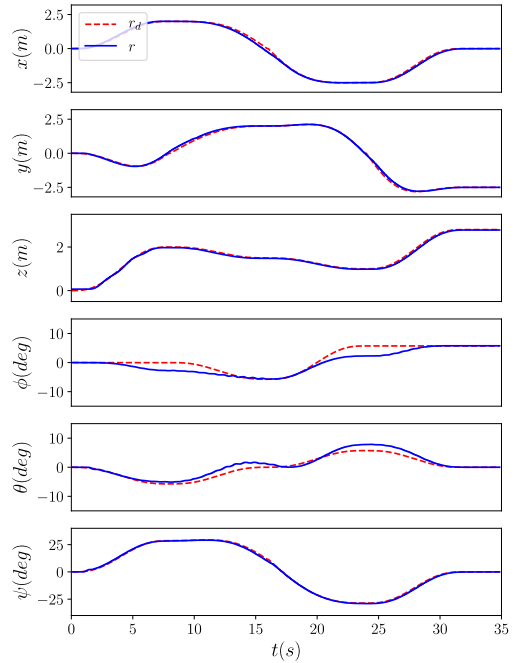


Fig. 16: The three types of structures used in our simulation.

Fig. 17: Simulation 1: A fully-actuated structure of 16 T -modules following a 6-DOF quintic-polynomial trajectoryFig. 18: Simulation 2: A fully-actuated structure of 5 T -modules and 4 R -modules following a 6-DOF quintic-polynomial trajectory

The experimental results show a large positional error, which is consistent with our analysis. The fully-actuated structure composed of T -modules used in Experiment 4-6, on the other hand, can push the tilting angle along roll or pitch to over 35° without losing stability, even if some motors saturate. This is specifically shown in Experiment 5. We design a generalized controller in Section VI based on the geometric controller by Lee et al. [11], which achieves exponential stability. In practice, the thrust force of a rotor has a limited range, which can affect the stability of a multi-rotor vehicle. We deal with this problem by taking the limits into consideration when designing the trajectory. A problem worth exploring in the future concerning this limit is how to guarantee stability under practical constraints when using geometric controllers for different structure configurations.

In general, the structure composed of T -modules attains better stability at higher tilting angles in comparison to the

one composed of R -modules. However, we also notice an issue related to the modeling of the structure. In Fig. 13 and 14, the attitude change affects the quality of position tracking, especially along z -axis. While conserving stability, the position tracking drifts along all three axes as the tilting angle increases. The drifting is due to the mismatch between the modeling and the physical multi-rotor construction. In (5), we show that the design matrix \mathbf{A} depends on the positions of the motors, which is not directly measurable, and has more impact on a T -module than on a R -module, or a traditional quadrotor. Specifically, the thrusting force of each rotor applies directly at the position of the motor mounts in our model, which may be different from the actual force as a result of the aerodynamic properties of the rotors. We address this problem by applying an integral term in the controller, which mitigates the drifting behavior by time as can be observed in Fig. 15 on

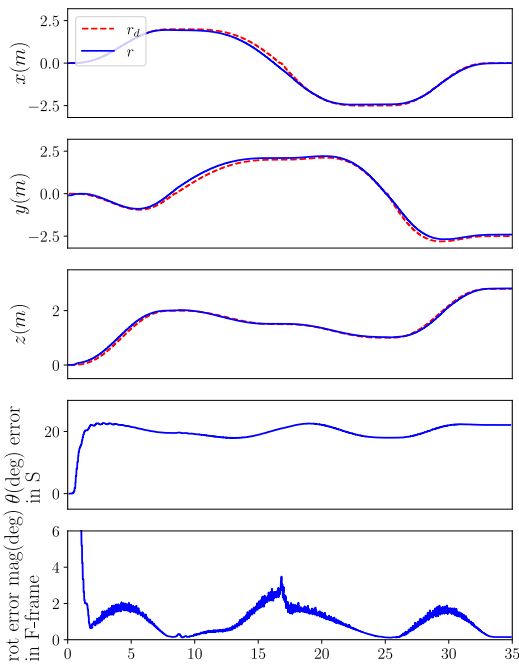


Fig. 19: Simulation 3: A fully-actuated structure of 3 T -modules and 2 R -modules, of which the F -frame and $\{S\}$ are not aligned, following a 6-DOF quintic-polynomial trajectory.

z -axis around time stamp 50.0 s.

On the simulation side, we focus on driving large heterogeneous structures with the proposed control strategy under different testing purposes. On one hand, as the number of modules increases along one axis, the inertia along that axis increases at a cubic rate according to parallel axis theorem, while the structure’s capability of generating torques increases at a quadratic rate. This results in a structure with more modules consume more power in total and in average. They also tend to possess less dexterity along the axis orthogonal to the plane that contains more modules. Assembling T -modules to a structure helps improve this drawback, as they generate torques along all axes despite their positioning. R -modules and traditional quadrotors contribute more force along certain directions more efficiently. Combining different types of modules offers a versatile solution to satisfy different task requirements. On the other hand, we introduce structural deformation in Simulation 1 to emulate the non-rigid module connections in a large structure. Such deformation leads to mismatch between calculated motor dynamics and the real motor dynamics. The simulation shows that although the attitude error becomes noisy, the structure is still able to maintain a low positional error and stay stable along the trajectory. We additionally provide a non-trivial example structure whose F -frame is not aligned with $\{S\}$. It is able to follow the trajectory using its F -frame instead of $\{S\}$.

VIII. CONCLUSION AND FUTURE WORK

In this work, we proposed a modular UAV that can increase its strength and ADOF from 4 to 5 and 6. We present two module designs, R - and T -module, both of which are

torque-balanced. The combination of the heterogeneous team of modules determines the number of ADOF. We modelled the actuation capabilities of the structures using the actuation ellipsoid actuation polytope. The polytope provides analyzing tools to check whether a structure can satisfy certain tasks requirements such as hovering at a certain tilting angle. We extend the concept of the actuation ellipsoid to find the best frame for a structure to hover and translate efficiently. We propose a generalized control policy for vehicles with 4, 5, and 6 ADOF. The experiments in real robots show our prototypes of R - and T -modules, and demonstrate that our controller works for vehicles with 4, 5, and 6 ADOF. With the increased number of ADOF, the vehicle can perform the independent motion in translation and rotation. The simulation in CoppeliaSim shows the scalability of the modular heterogeneous system.

For future work, we want to explore more possibilities in motion for the modular system such as omnidirectionality. Also, as different structure configurations satisfy different task requirements, we want to study systematic approaches to generate suitable structure designs given task requirements and available modules.

REFERENCES

- [1] I. H. Beloev, “A review on current and emerging application possibilities for unmanned aerial vehicles,” *Acta Technologica Agriculturae*, vol. 19, no. 3, pp. 70–76, 2016. [Online]. Available: <https://doi.org/10.1515/ata-2016-0015>
- [2] A. Gurtner, D. G. Greer, R. Glasscock, L. Mejias, R. A. Walker, and W. W. Boles, “Investigation of fish-eye lenses for small-uav aerial photography,” *IEEE Transactions on Geoscience and Remote Sensing*, vol. 47, no. 3, pp. 709–721, 2009.
- [3] D. K. Villa, A. S. Brandao, and M. Sarcinelli-Filho, “A survey on load transportation using multirotor uavs,” *Journal of Intelligent & Robotic Systems*, vol. 98, pp. 267–296, 2020.
- [4] D. Mellinger, M. Shomin, N. Michael, and V. Kumar, “Cooperative grasping and transport using multiple quadrotors,” *Springer Tracts in Advanced Robotics*, vol. 83 STAR, pp. 545–558, 2012.
- [5] Y. Li and C. Liu, “Applications of multirotor drone technologies in construction management,” *International Journal of Construction Management*, vol. 19, no. 5, pp. 401–412, 2019. [Online]. Available: <https://doi.org/10.1080/15623599.2018.1452101>
- [6] P. Liu, A. Chen, Y.-N. Huang, J.-Y. Han, J.-S. Lai, S.-C. Kang, T.-H. R. Wu, M.-C. Wen, and M.-H. Tsai, “A review of rotorcraft unmanned aerial vehicle (uav) developments and applications in civil engineering,” *SMART STRUCTURES AND SYSTEMS*, vol. 13, pp. 1065–1094, 06 2014.
- [7] F. Ruggiero, V. Lippiello, and A. Ollero, “Aerial manipulation: A literature review,” *IEEE Robotics and Automation Letters*, vol. 3, no. 3, pp. 1957–1964, 2018.
- [8] I. Maza, K. Kondak, M. Bernard, and A. Ollero, “Multi-uav cooperation and control for load transportation and deployment,” in *Selected papers from the 2nd International Symposium on UAVs, Reno, Nevada, USA June 8–10, 2009*. Springer, 2009, pp. 417–449.
- [9] F. Sabatino, “Quadrotor control: modeling, nonlinear control design, and simulation,” 2015.
- [10] S. Bouabdallah, “Design and control of quadrotors with application to autonomous flying,” p. 155, 2007. [Online]. Available: <http://infoscience.epfl.ch/record/95939>
- [11] T. Lee, M. Leok, and N. H. McClamroch, “Geometric tracking control of a quadrotor uav on $se(3)$,” in *49th IEEE Conference on Decision and Control (CDC)*, 2010, pp. 5420–5425.
- [12] D. Mellinger and V. Kumar, “Minimum snap trajectory generation and control for quadrotors,” in *2011 IEEE International Conference on Robotics and Automation*, 2011, pp. 2520–2525.
- [13] A. Alaimo, V. Artale, C. Milazzo, A. Ricciardello, and L. Trefiletti, “Mathematical modeling and control of a hexacopter,” in *2013 International Conference on Unmanned Aircraft Systems (ICUAS)*. IEEE, 2013, pp. 1043–1050.

- [14] D. Saldaña, B. Gabrich, G. Li, M. Yim, and V. Kumar, "Modquad: The flying modular structure that self-assembles in midair," in *2018 IEEE International Conference on Robotics and Automation (ICRA)*, 2018, pp. 691–698.
- [15] S. Rajappa, M. Ryll, H. H. Bühlhoff, and A. Franchi, "Modeling, control and design optimization for a fully-actuated hexarotor aerial vehicle with tilted propellers," in *2015 IEEE International Conference on Robotics and Automation (ICRA)*, 2015, pp. 4006–4013.
- [16] M. Zhao, T. Anzai, F. Shi, X. Chen, K. Okada, and M. Inaba, "Design, modeling, and control of an aerial robot dragon: A dual-rotor-embedded multilink robot with the ability of multi-degree-of-freedom aerial transformation," *IEEE Robotics and Automation Letters*, vol. 3, no. 2, pp. 1176–1183, 2018.
- [17] A. Franchi, R. Carli, D. Bicego, and M. Ryll, "Full-pose tracking control for aerial robotic systems with laterally bounded input force," *IEEE Transactions on Robotics*, vol. 34, no. 2, pp. 534–541, 2018.
- [18] M. J. Duffy and T. C. Samaritano, "The lift! project—modular, electric vertical lift system with ground power tether," in *33rd AIAA Applied Aerodynamics Conference*, 2015, p. 3013.
- [19] R. Oung and R. D'Andrea, "The distributed flight array," *Mechatronics*, vol. 21, no. 6, pp. 908–917, 2011.
- [20] H. Yang, S. Park, J. Lee, J. Ahn, D. Son, and D. Lee, "Lasdra: Large-size aerial skeleton system with distributed rotor actuation," in *2018 IEEE International Conference on Robotics and Automation (ICRA)*, May 2018, pp. 7017–7023.
- [21] M. Zhao, K. Kawasaki, T. Anzai, X. Chen, S. Noda, F. Shi, K. Okada, and M. Inaba, "Transformable multirotor with two-dimensional multilinks: Modeling, control, and whole-body aerial manipulation," *The International Journal of Robotics Research*, vol. 37, no. 9, pp. 1085–1112, 2018.
- [22] B. Gabrich, D. Saldaña, V. Kumar, and M. Yim, "A flying gripper based on cuboid modular robots," 05 2018.
- [23] K. Gilpin and D. Rus, "Modular robot systems," *IEEE robotics & automation magazine*, vol. 17, no. 3, pp. 38–55, 2010.
- [24] K. Stoy, D. Brandt, D. J. Christensen, and D. Brandt, "Self-reconfigurable robots: an introduction," 2010.
- [25] J. Xu, D. S. D'Antonio, and D. Saldaña, "H-modquad: Modular multirotors with 4, 5, and 6 controllable dof," in *2021 IEEE International Conference on Robotics and Automation (ICRA)*, 2021, pp. 190–196.
- [26] C. Holda, B. Ghalamchi, and M. W. Mueller, "Tilting multicopter rotors for increased power efficiency and yaw authority," in *2018 International Conference on Unmanned Aircraft Systems (ICUAS)*, 2018, pp. 143–148.
- [27] M. Allenspach, K. Bodie, M. Brunner, L. Rinsoz, Z. Taylor, M. Kamel, R. Siegwart, and J. Nieto, "Design and optimal control of a tiltrotor micro-aerial vehicle for efficient omnidirectional flight," *The International Journal of Robotics Research*, vol. 39, no. 10-11, pp. 1305–1325, 2020. [Online]. Available: <https://doi.org/10.1177/0278364920943654>
- [28] M. Ryll, G. Muscio, F. Pierri, E. Cataldi, G. Antonelli, F. Caccavale, and A. Franchi, "6d physical interaction with a fully actuated aerial robot," in *2017 IEEE International Conference on Robotics and Automation (ICRA)*, 2017, pp. 5190–5195.
- [29] S. Kalouche, "Goat: A legged robot with 3d agility and virtual compliance," in *2017 IEEE/RSJ International Conference on Intelligent Robots and Systems (IROS)*, 2017, pp. 4110–4117.
- [30] M. Hamandi, F. Usai, Q. Sablé, N. Staub, M. Tognon, and A. Franchi, "Design of multirotor aerial vehicles: A taxonomy based on input allocation," *The International Journal of Robotics Research*, vol. 40, no. 8-9, pp. 1015–1044, 2021. [Online]. Available: <https://doi.org/10.1177/02783649211025998>
- [31] D. Brescianini and R. D'Andrea, "Design, modeling and control of an omni-directional aerial vehicle," in *2016 IEEE International Conference on Robotics and Automation (ICRA)*, 2016, pp. 3261–3266.
- [32] M. Tognon and A. Franchi, "Omnidirectional aerial vehicles with unidirectional thrusters: Theory, optimal design, and control," *IEEE Robotics and Automation Letters*, vol. 3, no. 3, pp. 2277–2282, 2018.
- [33] M. Hamandi, K. Sawant, M. Tognon, and A. Franchi, "Omni-plus-seven (o7+): An omnidirectional aerial prototype with a minimal number of unidirectional thrusters," in *2020 International Conference on Unmanned Aircraft Systems (ICUAS)*, 2020, pp. 754–761.
- [34] M. Ryll, H. H. Bühlhoff, and P. R. Giordano, "Modeling and control of a quadrotor uav with tilting propellers," in *2012 IEEE International Conference on Robotics and Automation*, 2012, pp. 4606–4613.
- [35] M. Ryll, D. Bicego, and A. Franchi, "Modeling and control of fast-hex: A fully-actuated by synchronized-tilting hexarotor," in *2016 IEEE/RSJ International Conference on Intelligent Robots and Systems (IROS)*, 2016, pp. 1689–1694.
- [36] R. Oung, F. Bourgault, M. Donovan, and R. D'Andrea, "The distributed flight array," in *2010 IEEE International Conference on Robotics and Automation*, 2010, pp. 601–607.
- [37] R. Oung and R. D'Andrea, "The distributed flight array: Design, implementation, and analysis of a modular vertical take-off and landing vehicle," *The International Journal of Robotics Research*, vol. 33, no. 3, pp. 375–400, 2014. [Online]. Available: <https://doi.org/10.1177/0278364913501212>
- [38] K. Garanger, J. Epps, and E. Feron, "Modeling and experimental validation of a fractal tetrahedron uas assembly," in *2020 IEEE Aerospace Conference*, 2020, pp. 1–11.
- [39] Z. Wu, R. Zhao, M. Yu, Y. Zhao, W. Yang, W. Zhang, and F. Li, "Design, modeling and control of a composable and extensible drone with tilting rotors," in *2022 IEEE/RSJ International Conference on Intelligent Robots and Systems (IROS)*, 2022, pp. 12 682–12 689.
- [40] R. M. Murray, S. S. Sastry, and L. Ze-xiang, "A mathematical introduction to robotic manipulation," 1994.
- [41] R. Ortega and M. Spong, "Adaptive motion control of rigid robots: a tutorial," in *Proceedings of the 27th IEEE Conference on Decision and Control*, 1988, pp. 1575–1584 vol.2.
- [42] T. Yoshikawa, "Manipulability of robotic mechanisms," *The international journal of Robotics Research*, vol. 4, no. 2, pp. 3–9, 1985.
- [43] M. Allenspach, K. Bodie, M. Brunner, L. Rinsoz, Z. Taylor, M. Kamel, R. Siegwart, and J. Nieto, "Design and optimal control of a tiltrotor micro-aerial vehicle for efficient omnidirectional flight," *The International Journal of Robotics Research*, vol. 39, no. 10-11, pp. 1305–1325, 2020. [Online]. Available: <https://doi.org/10.1177/0278364920943654>
- [44] P. Yu, Y. Su, M. J. Gerber, L. Ruan, and T.-C. Tsao, "An over-actuated multi-rotor aerial vehicle with unconstrained attitude angles and high thrust efficiencies," *IEEE Robotics and Automation Letters*, vol. 6, no. 4, pp. 6828–6835, 2021.
- [45] S. Boyd, S. P. Boyd, and L. Vandenberghe, *Convex optimization*. Cambridge U. press, 2004.
- [46] F. Borrelli, A. Bemporad, and M. Morari, *Predictive control for linear and hybrid systems*. Cambridge University Press, 2017.
- [47] J. Xu and D. Saldaña, "Finding optimal modular robots for aerial tasks," in *2023 IEEE International Conference on Robotics and Automation (ICRA)*, 2023, pp. 11 922–11 928.
- [48] D. S. D'Antonio, G. A. Cardona, and D. Saldaña, "The catenary robot: Design and control of a cable propelled by two quadrotors," *IEEE Robotics and Automation Letters*, vol. 6, no. 2, pp. 3857–3863, 2021.
- [49] W. Höning and N. Ayanian, *Flying Multiple UAVs Using ROS*. Springer International Publishing, 2017, pp. 83–118.
- [50] M. W. Mueller, M. Hamer, and R. D'Andrea, "Fusing ultra-wideband range measurements with accelerometers and rate gyroscopes for quadcopter state estimation," in *2015 IEEE International Conference on Robotics and Automation (ICRA)*, 2015, pp. 1730–1736.
- [51] M. W. Mueller, M. Hehn, and R. D'Andrea, "Covariance correction step for kalman filtering with an attitude," *Journal of Guidance, Control, and Dynamics*, vol. 40, no. 9, pp. 2301–2306, 2017. [Online]. Available: <https://doi.org/10.2514/1.G000848>
- [52] P. Yedamale, "Brushless dc (bldc) motor fundamentals," *Microchip Technology Inc*, vol. 20, no. 1, pp. 3–15, 2003.
- [53] E. Rohmer, S. P. N. Singh, and M. Freese, "Coppeliassim (formerly v-rep): a versatile and scalable robot simulation framework," in *Proc. of The International Conference on Intelligent Robots and Systems (IROS)*, 2013, www.coppeliarobotics.com.
- [54] S. Macfarlane and E. A. Croft, "Jerk-bounded manipulator trajectory planning: design for real-time applications," *IEEE Transactions on robotics and automation*, vol. 19, no. 1, pp. 42–52, 2003.